CDF/ANAL/EXOTIC/CDFR/9575
Version 3.1
June 8, 2009

Setting Limits on GMSB Models using the $\gamma\gamma + \not\!\!E_T$ Final State[1]

Eunsin Lee and Dave Toback
Texas A&M University

Ray Culbertson and Sasha Pronko
Fermilab

Max Goncharov
MIT

Abstract

We present the results of an optimized search for a gauge mediated supersymmetry breaking (GMSB) model with $\tilde{\chi}_1^0 \rightarrow \gamma\tilde{G}$ with $\tau(\tilde{\chi}_1^0) = 0$ ns in the $\gamma\gamma+\not\!\!E_T$ final state. We observe 0 events using 2.59 fb^{-1} of data collected by the CDF II detector, which is consistent with the background estimate of 1.38 ± 0.44 events. We set cross section and mass limits as well as interpret our results for lifetimes up to 2 ns in the $\tilde{\chi}_1^0$ lifetime vs. mass plane with a mass reach of 149 GeV/c^2 at $\tau(\tilde{\chi}_1^0) = 0$ ns.

[1]This note supercedes the results in version 2.0 which was based on 2.0 fb^{-1} data and blessed on 11/06/2008. Differences are listed in appendix B. This note is now up to date and largely standalone.

Contents

1 Introduction

The $\gamma\gamma+\not\!\!E_T$ final state is present in many theoretical models of new physics beyond the Standard Model (SM) [1]. The most commonly discussed theory that would produce it is gauge mediated supersymmetry breaking (GMSB) [2] with $\tilde{\chi}_1^0 \rightarrow \gamma\tilde{G}$ where the $\tilde{\chi}_1^0$ is the lightest neutralino and the next-to-lightest supersymmetric particle (NLSP), and the $\tilde{G}$ is the supersymmetric partner of the graviton, the gravitino, and the lightest supersymmetric particle (LSP). GMSB models are compelling for both theoretical and experimental reasons [3]. As the messenger interactions are flavor-independent it intrinsically suppresses flavor-changing neutral currents and CP-violating processes to SM levels. For important parts of parameter space it is also consistent with cosmological constraints [4] as all SUSY particles produced in the early universe decay to the $\tilde{G}$ LSP which is then a warm dark matter candidate [5]. Finally, for much of this same parameter space this model naturally predicts $\tilde{\chi}_1^0 \rightarrow \gamma\tilde{G}$ which produces high energy photon+$\not\!\!E_T$ events at the Tevatron and gained favor with the appearance of the $ee\gamma\gamma\not\!\!E_T$ candidate event in Run I [6].

For these models current limits from collider experiments, astronomy and cosmology favor a heavy $\tilde{\chi}_1^0$, with a mass>100 GeV, and a lifetime on the order of nanoseconds or less that decays to $\gamma\tilde{G}$ [5]. These limits restrict the masses of the squarks and gluons to be so large that they are too heavy to be produced at the Tevatron, thus making gaugino pair-production channels dominate for much of the available parameter space accessable at the Tevatron [2]. In this case the decays produce a pair of $\tilde{\chi}_1^0$'s in association with other high energy particles, with each $\tilde{\chi}_1^0$ decaying into a $\tilde{G}$, that gives rise to $\not\!\!E_T$, and a photon. Depending on how many of the two $\tilde{\chi}_1^0$'s decay inside the detector, due to their large decay length, the event has the signature $\gamma\gamma+\not\!\!E_T$, $\gamma+\not\!\!E_T$ or $\not\!\!E_T$ with one or more additional high E_T particles. At CDF we separate the search for GMSB into short lifetime searches ($\tau < 2$ ns) and long lifetime searches, following the recommendations of Ref. [7]. Large lifetime searches in the delayed $\gamma + \not\!\!E_T + jet$ final state are described in [8]. In this note we focus on the optimization of the $\gamma\gamma+\not\!\!E_T$ final state, which is more sensitive to lower $\tilde{\chi}_1^0$ lifetimes which are favored for the large $\tilde{\chi}_1^0$ masses [7].

The structure of this note is as follows: This section continues with a description of GMSB models in more detail, summarizes the previous searches and provides an overview of our analysis and search strategy. Section 2 describes the dataset and the event preselection. Section 3 outlines the different backgrounds and how we estimate them for use in the optimization procedure. Section 4 describes the acceptance estimate using the Monte Carlo (MC) methods and Section 5 gives the systematic uncertainties on the acceptance and the production cross sections. The optimization procedure, and its result, are given in Section 6. We unblind the signal region in Section 7, compare with expectations and set cross section, mass and lifetime limits. We conclude in Section 8 with expectations for the future. Appendix A contains the versions of the figures for the PRL [9].

This is a revised note that supercedes the blessed (November 06, 2008) results based on 2.0 fb^{-1} data. Appendix B lists the changes to the analysis since the blessing and changes since the re-blessing (April 30, 2009). This version of the note contains the current status of the analysis and is largely standalone; all the numbers are up to date.

Λ	the effective SUSY breaking scale
M_m	the messenger mass scale
N	the number of messenger fields
$\tan\beta$	the ratio of the MSSM Higgs vacuum expectation values
sign(μ)	the sign of the Higgs sector mixing parameter
$C_{\tilde{G}}$	the $\tilde{G}$ mass factor

Table 1: The six parameters of the minimal model of GMSB.

1.1 Theory and Phenomenology

Supersymmetric models with GMSB provide an interesting alternative to the scenario in which the soft terms of the low-energy fields are induced by gravity [2]. These theories allow for a natural suppression of flavor violations in the supersymmetric sector and have very distinctive phenomenological features. In GMSB models the standard model gauge interactions act as the messengers of supersymmetry breaking if fields within the supersymmetry breaking sector transform under the standard model gauge group.

The minimal model of GMSB can be described in terms of the six free parameters listed in Table 1 [10]. The effective SUSY breaking scale, Λ, is important because it sets the overall mass scale of the supersymmetric particles. To first approximation all of the MSSM superpartner masses scale linearly with Λ. The number of messenger fields, N, is also very important because it determines which sparticle is the NLSP, typically either the stau, $\tilde{\tau}$, or the $\tilde{\chi}_1^0$ depending on parameter choice [10]. For $N = 1$ the NLSP is mainly the lightest neutralino, and for $N \geq 2$ it is the $\tilde{\tau}$. We will focus on the $\tilde{\chi}_1^0$-NLSP case here, for which the branching ratio is $\sim$100% to decay to a photon and a $\tilde{G}$ in our mass regime. While the NLSP lifetime scales with the gravitino scale factor, $C_{\tilde{G}}$, as well as $M_{\tilde{G}}$ [2], for much of the parameter space it is of the order of ns. The mass range with $M_{\tilde{G}}$ between a few hundred eV/c^2 and a few keV/c^2 is favored for cosmological reasons and typically produces a neutralino lifetime of less than a few hundred nanoseconds depending on the NLSP mass [5]. This parameter is important for our purposes because the lifetime determines whether the NLSP decays inside or outside the detector. For more discussion of the issues and details of prospects of searches with long-lived neutralinos-NLSPs which decay to $\gamma\tilde{G}$ see Ref. [7].

As there are many GMSB parameter combinations that match this phenomenology, representative "model lines" have been identified that cover specific characteristics of GMSB models with an $\tilde{\chi}_1^0$ NLSP with only one free parameter setting the particle masses. We choose the most commonly used for this analysis, the Snowmass Points and Slopes (SPS) model line 8 [10]: $N = 1$; $M_m/\Lambda = 2$; $\tan\beta = 15$; and $\mu > 0$, where Λ is a free parameter. We also take $C_{\tilde{G}}$ as a free parameter as it controls the $\tilde{G}$ mass. Taking these two model parameters is the equivalent of taking the $\tilde{\chi}_1^0$ mass, $m_{\tilde{\chi}_1^0}$, and lifetime, $\tau_{\tilde{\chi}_1^0}$, as free parameters. As calculated in Ref. [2] the $\tilde{\chi}_1^0$ lifetime, $\tau_{\tilde{\chi}_1^0}$, is given by

$$\tau_{\tilde{\chi}_1^0} = C \cdot \left(\frac{100 \text{ GeV}}{m_{\tilde{\chi}_1^0}}\right)^5 \cdot \left(\frac{m_{\tilde{G}}}{1 \text{ keV}}\right)^2 \text{ ns} \tag{1}$$

where $C = 69.33$, with $m_{\tilde{G}}$ in keV and $m_{\tilde{\chi}_1^0}$ in GeV. We will describe our analysis in terms of $m_{\tilde{\chi}_1^0}$ and $\tau_{\tilde{\chi}_1^0}$ for clarity of presentation and for use by future model builders.

For this model at the Tevatron, and taking into account current limits, $\tilde{\chi}_1^0$'s are mostly pair produced as end products of cascade decays from a chargino, $\tilde{\chi}_1^{\pm}$, pair (∼45% of all channels) or a $\tilde{\chi}_1^{\pm}$ and a $\tilde{\chi}_2^0$ (∼25% of all channels) [14]. The major decay channels are shown in Figure 1. Table 2 gives some example GMSB model parameters, the resulting $\tilde{\chi}_1^0$ masses and lifetimes, and the next-to-leading-order (NLO) production cross sections for our region of interest. The production cross sections are calculated to leading-order using PYTHIA [11] with the NLO corrections using the k-factors shown in Figure 2 as a function of $\tilde{\chi}_1^0$ masses for $\tilde{\chi}_1^{\pm}$ pair and $\tilde{\chi}_1^{\pm}\tilde{\chi}_2^0$ production as taken from [12]. The values range between 1.1-1.3 for the mass range considered. The production cross section is independent of the $\tilde{\chi}_1^0$ lifetime, as this only scales with the $\tilde{G}$ mass for a fixed $\tilde{\chi}_1^0$ mass [2]. To simulate the different $\tilde{\chi}_1^0$ masses we vary the SUSY breaking scale, Λ, and the messenger mass scale, M_m, but fix the ratio, $M_m/\Lambda = 2$. For our model we have $m_{\tilde{\chi}_1^{\pm}} \approx m_{\tilde{\chi}_2^0} \approx 1.9 \cdot m_{\tilde{\chi}_1^0}$. We use production from all process to estimate our sensitivity as it produces the best sensitivity to the model [13].

Since astronomical observation constraints restrict $m_{\tilde{G}}$ to be near a keV/c^2 [5], for much of the parameter space the $\tilde{\chi}_1^0$ can be long-lived from Eq. (1), with a decay time on the order of nanoseconds which corresponds to decay lengths of meters. The $\tilde{\chi}_1^0$ can decay inside the detector or, in a fraction of cases, leave the detector volume before it decays. This separates the following event signatures: $\gamma\gamma+\not\!\!E_T$, $\gamma+\not\!\!E_T$ or $\not\!\!E_T$, each in association with jets from the τ's in the cascade decays. In this note we will focus on the $\gamma\gamma+\not\!\!E_T$ case as this is more sensitive to low lifetimes, on the order of nanoseconds (<2 ns), which is favored for $m_{\tilde{\chi}_1^0} \gtrsim 100$ GeV for regions consistent with cosmology bands [7]. While we will take advantage of the other high energy final state particles procduced from the decays, we retain a model independent type analysis by not explicitly requiring the identification of taus. Next we outline our search strategy and the datasets.

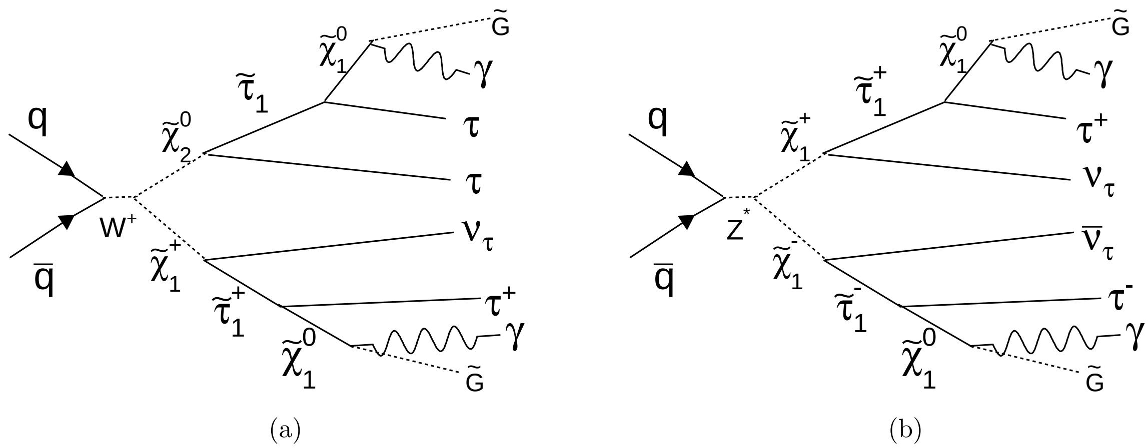

Figure 1: Feynman diagrams of the dominant tree production processes at the Tevatron for the GMSB model line we consider: $\tilde{\chi}_1^\pm \tilde{\chi}_2^0$ (45%) (a) and $\tilde{\chi}_1^\pm$ pair (b) production (25%). Note that we only show one choice for the charge. The remaining processes are slepton (τ_1, e_R, μ_R) pair production.

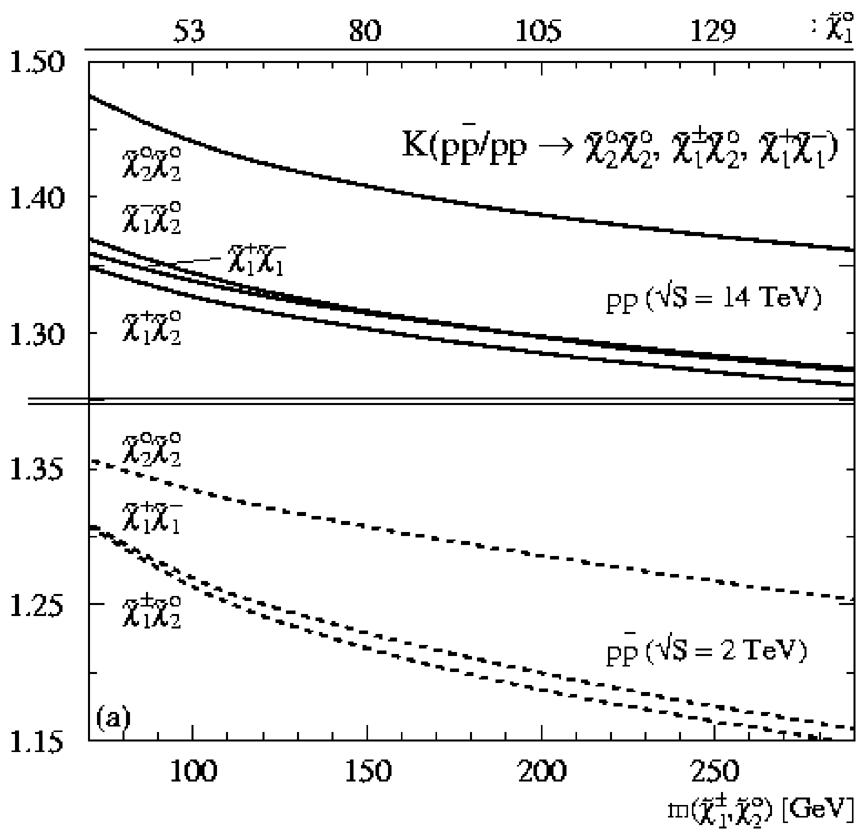

Figure 2: The k-factors for use in modifying the LO production cross sections of $\tilde{\chi}_1^\pm$ pair and $\tilde{\chi}_1^\pm \tilde{\chi}_1^0$ production as a function of the average mass of the $\tilde{\chi}_1^\pm$ and $\tilde{\chi}_2^0$ which are almost identical in the scenario chosen in Ref. [10]. The figure is taken from Fig. 3a of Ref. [12]. For convenience the $\tilde{\chi}_1^0$ mass is plotted as a second x-axis, taken from Fig. 3b therein.

$m_{\tilde{\chi}_1^0}$ (GeV/c^2)	$\tau_{\tilde{\chi}_1^0}$ (ns)	$m_{\tilde{G}}$ (eV/c^2)	Λ (TeV)	k-factor	NLO σ_{prod} (fb)
70	0	1.38	53.5	1.23	999.9
90	0	2.18	67.2	1.20	286.8
100	0	2.63	74.0	1.19	169.0
130	0	4.34	95.0	1.16	36.23
130	2	317	95.0	1.16	36.23
140	0	4.99	101.8	1.15	22.97
150	0	5.7	108.8	1.14	14.54

Table 2: Examples of $\tilde{\chi}_1^0$ masses and lifetimes relevant for this analysis and their translation to the SUSY parameters in accordance with the GMSB SPS model line 8 [10]. To get different $\tilde{\chi}_1^0$ masses we vary the SUSY breaking scale, Λ, and the messenger mass scale, M_m, but fix the ratio, $M_m/\Lambda = 2$. Also given are the NLO production cross sections. Note that the production cross section is independent of the $\tilde{\chi}_1^0$ lifetime. Also note that since we are not yet sensitive to the cosmology favored region, $m_{\tilde{G}} \approx 1$ keV, we are focusing on $\tau_{\tilde{\chi}_1^0} = 0$ cases.

1.2 Previous Searches

There have been many previous searches for anomalous $\gamma\gamma+\not\!\!E_T$ production including Run I searches from CDF [6] and DØ [15] and multiple searches from LEP II [16]. The most recent published search from CDF in the $\gamma\gamma+\not\!\!E_T$ final state at CDF was with 202 pb^{-1} of data [17]. With zero observed events with $\not\!\!E_T>$ 45 GeV on a background of 0.27±0.12 and an 18% systematic error we set a 3.3 event 95% C.L. upper limit on the expected number of signal events. Using the NLO predictions we set a limit of $M_{\tilde{\chi}_1^0} > 93$ GeV/c^2, assuming the $\tilde{\chi}_1^0$ lifetime is zero. The current most sensitive search for GMSB with $\tau = 0$ is from DØ using 1.1 fb^{-1} of data [18]. The observed upper limits are $M_{\tilde{\chi}_1^0} > 125$ GeV/c^2.

In 2006 a CDF search [19] for a single photon with delayed arrival time, using the EMTiming system [20], at least one jet, and $\not\!\!E_T$, set the most stringent limits on GMSB for nanosecond lifetimes and large masses of the $\tilde{\chi}_1^0$'s. The search found 2 events using 570 pb^{-1} of data, which was consistent with the background estimate of 1.3±0.7 events. Figure 3 shows the exclusion region in the $\tilde{\chi}_1^0$ lifetime vs. mass plane with a mass reach of 101 GeV/c^2 at $\tau_{\tilde{\chi}_1^0}$ =5 ns. This results extended the world sensitivity to these models beyond those from LEP II, which searched for non-zero $\tilde{\chi}_1^0$ lifetimes using photon pointing [16].

1.3 Overview of the Analysis

This analysis is designed to extend the search range to GMSB models in the $\gamma\gamma + \not\!\!E_T$ final state with $\tau = 0$ to higher masses since the same analysis is sensitive for $\tau \lesssim 2$ ns. We estimate our sensitivity there for larger lifetimes as well. The search is designed to identify the $\gamma\gamma + \not\!\!E_T$ events from the cascade decays from $\tilde{\chi}_1^{\pm}$ and/or $\tilde{\chi}_2^0$. The new features of our analysis since the last $\gamma\gamma + \not\!\!E_T$ search with 202 pb^{-1} are the following:

- Use the EMTiming system [20] to reject cosmic rays and beam halo backgrounds.
- Use a new *Met Resolution Model* [21] to improve QCD background rejection.
- Simplify and re-optimize the analysis due to more direct ways of rejecting backgrounds.
- Use 13 times the data (2.6 fb^{-1}).
- Estimate the sensitivity for $\tau_{\tilde{\chi}_1^0} \lesssim 2$ ns.

The analysis begins by examining events with two isolated, central ($|\eta| \lesssim 1.0$) photon candidates with $E_T > 13$ GeV. All events are required to pass global event selection, photon ID and isolation requirements, and pass non-collision background rejection requirements. This set of cuts defines our preselection sample, which is dominated by QCD events ($\gamma\gamma$, $\gamma - jet \rightarrow \gamma\gamma_{fake}$ and $jet - jet \rightarrow \gamma_{fake}\gamma_{fake}$). Events with $\not\!\!E_T$ are typically QCD with fake $\not\!\!E_T$, electroweak events with real $\not\!\!E_T$ (e.g., $W\gamma \rightarrow e\nu\gamma \rightarrow \nu\gamma_{fake}\gamma$) and non-collision backgrounds such as PMT spikes, cosmic rays, and beam-halo (B.H.) interactions.

We perform an *a priori* analysis in the sense that we blind the signal region and select the final event requirements based on the signal and background expectations alone. The final signal region is defined by further kinematic cuts, including significant $\not\!\!E_T$ and large H_T, where H_T is defined as the sum of E_T of the two photons, any jets with $E_T > 15$ GeV and $|\eta| < 2.4$, any electrons with $E_T > 13$ GeV with fiducial requirements only, and the $\not\!\!E_T$. With these cuts we optimize the rejection of the remaining backgrounds while retaining acceptance for our signal. In Section 6 we detail the optimization procedure and give the predicted sensitivity using a simulation of our GMSB model (see Section 4) and calculate, for each GMSB parameter point, the lowest expected 95% C.L. cross section limit as a function of these variables. After this procedure we are left with an optimal, robust set of requirements that define the signal region.

In addition to setting limits on $\tau = 0$ decays, we investigate our sensitivity for the lifetime region $\tau \lesssim 2$ ns to complement the delayed photon analysis [19]. As shown in Figure 3 there is an uncovered region below about a ns.

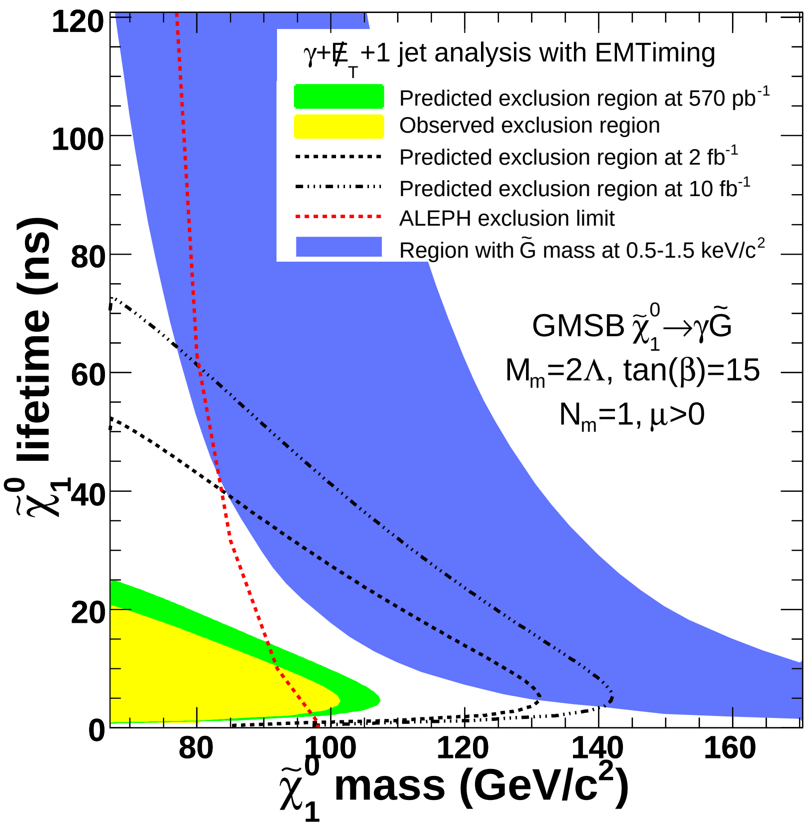

Figure 3: The predicted and observed exclusion region from the delayed photon search in the $\gamma + \not\!\!E_T$+jet final state, taken from Ref. [19], along with cosmology favored region and the exclusion limit from ALEPH/LEP [16]. Note that this figure has been fixed for the incorrect cosmology favored region calculation. For more detials see Appendix B.

2 Triggers, Datasets and Object ID

In this section we describe the trigger, dataset, and the object ID used to create the preselection sample. The analysis is based on data collected from the beginning of Run II starting with run 190851 (December 7, 2004), after the EMTiming system became available, and up to run 261005 (April 16, 2008). The integrated luminosity is obtained from the offline database and is scaled by the standard 1.019 correction factor [22]. To ensure the quality of data, the good run list v.23 [23] for the *Photon* group is applied. It requires good CAL, SMX, COT (COT degraded period is allowed, but Silicon is required during that period). After all requirements we are left with 2.59$\pm$0.16 fb^{-1} of data [24] for periods 1 to 17.

To get the preselection sample we select a set of events that pass the photon triggers, photon ID and isolation, phoenix rejection, vertex requirements and re-assignment (vertex swap), non-collision removal cuts, and $\not\!\!E_T$ cleanup cuts; all given in Tables 3-8. At the end we are left with a sample of 38,053 events, as described in Table 9. Next we describe each of the cuts in more detail.

2.1 Triggers and Datasets

The events used in this analysis are required to pass one of the DIPHOTON_12 (iso), DIPHOTON_18 (no-iso), PHO_50 (no-iso) or PHO_70 (no-hadem) triggers[25]. The PHO_50 and PHO_70 triggers are added to recover potential loss in efficiency for $\chi^2_{\rm CES}$ at high photon E_T[26]. The requirements for each at the three trigger levels are listed in Table 3. The $\gamma\gamma + X$ data are "ntuplized" in the "cdfpstn:cdipad,h,i,j" Stntuples. We use the Stntuple dev_243 [27] and version 6.1.4 of the cdfsoft2 release.

2.2 Diphoton Samples and Object ID

Diphoton candidate events are selected from the subsample of events that pass one of the triggers. Both leading photons are required to be in the fiducial part of the central, $|\eta| \leq 1.1$, have $E_T^\gamma > 13$ GeV, and pass the standard photon ID and isolation requirements, with two additional ID requirements. The trigger efficiency after all offline cuts, for our signal, is taken to be 100% for these cuts [28]. The full set of ID and isolation requirements are given in Table 4.

In addition to the standard photon ID and isolation cuts [29] we have two additional cuts to suppress both $e\gamma$ events where an electron fakes a prompt photon [30] and fake photons from PMT spikes [31]. Since an important source of background with large real $\not\!\!E_T$ is $W\gamma \to e\gamma + \not\!\!E_T \to \gamma\gamma_{fake} + \not\!\!E_T$ events where an electron fakes a prompt photon we have added Phoenix rejection cuts [30] to the list of photon ID cuts. In many cases such a photon is either due to a bremsstrahlung in the detector material in front of the COT or due to a lost track (see Ref. [30] for details). These electrons usually leave a few silicon hits and can be reconstructed by the Phoenix tracking algorithm. We reject an event if either of the two photons is matched to a Phoenix track. PMT spikes in the CEM calorimeter can produce a fake photon signature and give fake $\not\!\!E_T$. To suppress this background we remove events if either photon candidate has a large PMT asymmetry: $A = |pmt1 - pmt2|/(pmt1 + pmt2)$,

DIPHOTON_12	
L1	Single tower $E_T > 8$ GeV ($z = 0$) Single tower Had/EM< 0.125 unless $E_T > 14$ GeV
L2	Two high E_T pass clusters, $E_T > 10$ GeV ($z = 0$), $\eta < 3.6$ Both clusters Had/EM < 0.125 Both clusters Iso < 3 || Iso $< 0.15E_T$
L3	Two L3 clusters, $E_T > 12$ GeV ($z = 0$) Both clusters Had/EM $< 0.055 + 0.00045E$ || $E_T > 200\ GeV$ Both clusters Iso(cone 0.4) < 2 || $< 0.10E_T$ for central, average and scaled CES $\chi^2 < 20$
DIPHOTON_18	
L1	Single tower $E_T > 8$ GeV ($z = 0$) Single tower Had/EM< 0.125 unless $E_T > 14$ GeV
L2	Two high E_T pass clusters, $E_T > 16$ GeV ($z = 0$), $\eta < 3.6$ Both clusters Had/EM< 0.125
L3	Two L3 clusters, $E_T > 18$ GeV ($z = 0$) Both clusters Had/EM $< 0.055 + 0.00045E$ || $E_T > 200$ GeV for central, average and scaled CES $\chi^2 < 20$
PHO_50	
L1	Single tower $E_T > 8$ GeV ($z = 0$) Single tower Had/EM< 0.125 unless $E_T > 14$ GeV
L2	$E_T > 40$ GeV Had/EM< 0.125
L3	$E_T > 50$ GeV Had/EM< 0.125 (for $E < 200$ GeV)
PHO_70	
L1	Single tower EM+Had $E_T > 10$ GeV ($z = 0$) Single tower Had/EM< 0.125 unless $E_T > 14$ GeV
L2	$E_T > 70$ GeV
L3	$E_T > 70$ GeV Had/EM$< 0.2 + 0.001E$ (for $E < 100$ GeV)

Table 3: The triggers used to create the diphoton sample. The PHO_50 and PHO_70 triggers are added to the standard diphoton triggers to recover loss in efficiency of χ^2_{CES} at high E_T^{γ}. We only require an event to pass one of these triggers.

The Standard Photon ID and Isolation Cuts	
detector	CEM
corrected E_T	$\geq$ 13 GeV
CES fiduciality	$\lvert X_{\mathrm{CES}}\rvert \leq 21$ cm 9 cm $\leq \lvert Z_{CES}\rvert \leq$ 230 cm
average CES χ^2	$\leq$20
Had/Em	$\leq$0.055+0.00045$\times E$
corrected CalIso0.4	$\leq$0.1$\times E_T$ if E_T<20 GeV or $\leq 2.0+0.02\times(E_T - 20)$
TrkIso0.4	$\leq 2.0 + 0.005 \times E_T$
$N3D$ tracks in cluster	≤ 1
track P_T if $N3D = 0$	$\leq$1.0+0.005$\times E_T$
E_T of 2^{nd} CES cluster (wire and strip)	$\leq$0.14$\times E_T$ if E_T<18 GeV $\leq$2.4+0.01$\times E_T$ if $E_T\geq$18 GeV
Additional Photon ID Cuts	
Phoenix	Reject photons matched to a Phoenix track
PMT Asymmetry	$A = \lvert pmt1 - pmt2\rvert/(pmt1 + pmt2) < 0.65$

Table 4: Summary of the photon ID and isolation cuts. These are the standard cuts with the addition of Phoenix rejection and PMT asymmetry cuts.

where $pmt1$ and $pmt2$ are the energies reported from PMT-1 and PMT-2, respectively.

All diphoton candidate events are required to pass a set of global requirements. To help maintain the projective nature of the calorimeter we select events with at least one vertex of class 12 with $|Z_{vx}| \leq$60 cm. The E_T of all calorimeter objects (individual towers, photons, electrons, jets and $\not\!\!E_T$) are calculated with respect to the highest $\sum P_T$ vertex. However, in some events the vertex our algorithm chooses is the wrong vertex, for example, when a $\gamma\gamma$ pair is produced by one interaction and overlaps with a more energetic semi-hard interaction (often referred to as a Min-Bias interaction) that produces the highest $\sum P_T$ vertex. A wrong vertex choice results in mis-measured E_T of both photon candiates, thus it causes fake $\not\!\!E_T$. Although this mis-measurement is small in most cases, sometimes it can give a very large value of fake $\not\!\!E_T$ if the two vertices are far apart or if the photons are very energetic. Fortunately, this effect can be easily corrected for most events by a vertex re-assignment procedure. For every event we calculate the photon E_T and $\not\!\!E_T$ for every vertex of class 12 with $|Z_{vx}| \leq$60 cm and correct the $\not\!\!E_T$ for this difference. If it produces a smaller $\not\!\!E_T$ value we take these new values of the photon E_T and $\not\!\!E_T$, and use then these values instead of the primary vertex values in the kinematic calculations. These well defined variables are used for signal and background calculations with identical procedures. As a result of this procedure some photons fall below the $E_T^{\gamma} \geq$13 GeV threshold and are removed from the final sample. Events that start with E_T^{γ} <13 GeV are not added back. The standard vertex requirements, with vertex re-assignment, are listed in Table 5.

Additional requirements are placed on the sample to reduce non-collision backgrounds. Muons from beam halo are known to fake photon candidates [31, 32]. Because such events

Vertex Requirements
At least one vertex of class 12 with $\lvert Z_{vx}\rvert \leq$60 cm
The highest $\sum P_T$ vertex is selected as a primary vertex
For events with multiple vertices: Calculate the photon E_T and $\not\!\!E_T$ for every vertex with $\lvert Z_{vx}\rvert \leq$60 cm Correct the E_T for for this change Take these new values of the photon E_T and the $\not\!\!E_T$ if the $\not\!\!E_T$ is smaller

Table 5: Summary of the vertex requirements and vertex re-assignment algorithms.

are not related to a hard interaction and usually appear only in one calorimeter wedge, they also create large $\not\!\!E_T$. The dominant background from this source is when the beam halo muon(s) produce both photons. Events with a single beam halo candidate overlapping with a SM $\gamma + jet$ event have been shown to be negligible and we have ignored them here [21]. To suppress contributions due to this background, events are rejected if both photons are identified as beam halo candidates, using the beam halo ID cuts in Table 6 [32], and separated by $|\Delta\phi| < 30^\circ$ (within neighboring wedges).

A photon is identified as being from Beam Halo if	
Cuts	values
seedWedge	>9
NHadPlug	>2
seedWedgeHadE	$< [0.4 + (0.019(N_{vx12} - 1) + 0.013)\text{seedWedge}]$ GeV
wedge number	0 or 23

Table 6: Summary of the requirements to identify photons from beam halo sources. For more detail see Ref. [32]. Events are rejected if both photons are identified as beam halo candidates and are separated by $|\Delta\phi| < 30°$.

A cosmic ray muon that traverses the detector can also help fake the $\gamma\gamma + \not\!\!E_T$ signature. These events can mostly be rejected based on their time of arrival in the calorimeter; cosmics are not correlated in time with collisions, and therefore their arrival time distribution is roughly flat. If the cosmic ray created both photons then the difference in arrival time of the first and second photons from cosmic rays is also proportional to the spatial separation between these two photons; photons from collision events arrive almost coincidentially in time. Thus, to suppress contributions from cosmic ray sources, we use the EMTiming system [20] to apply timing cuts to reject an event if either photon is more than 4σ from being consistent with coming from the interaction or if the two photons are well separated in time [31, 32]. The cosmic ray rejection cuts are listed in Table 7.

The last set of global cuts we apply are the $\not\!\!E_T$ cleanup cuts to remove events where the $\not\!\!E_T$ is likely to be due to a severe energy mis-measurement of a photon or jet. Such cases include the so-called *Tower-9* effect [33], energy lost in ϕ-cracks between CEM towers, or when a photon (or π^0) is lost in the central or forward crack leaving only a signature of a small jet. Therefore, we reject an event if the second photon or any jet is pointing right at the $\not\!\!E_T$. The full set of $\not\!\!E_T$ cleanup cuts are listed in Table 8.

An event is identified as a cosmic ray if
Either $\lvert T_{\gamma 1}\rvert$ or $\lvert T_{\gamma 2}\rvert > 4\sigma_T$, where $\sigma_T = 1.665$ ns
or $\lvert \Delta T_{\gamma\gamma} = T_{\gamma 1} - T_{\gamma 2}\rvert > 4\sigma_{\Delta T}$, where $\sigma_{\Delta T} = 1.021$ ns

Table 7: Summary of the EMTiming cuts to remove cosmic ray events. T_γ is the EMTiming recorded value with only slewing corrections [20].

Case	The event is removed if
For 2nd photon with $\Delta\phi(\not\!\!E_T - \gamma 2) < 0.3$	$\lvert\eta_{det}(\gamma 2)\rvert > 1.0$ or $\lvert\eta_{det}(\gamma 2)\rvert < 0.1$ or $\lvert X_{CES}(\gamma 2)\rvert > 18.5$ cm
For any jet ($\lvert\eta_{det}(jet)\rvert < 2.5$, $E_T > 5$ GeV, $N_{twr} < 10$, $N_{trk} < 5$) with $\Delta\phi(\not\!\!E_T - jet) < 0.3$	$EmFr > 0.875$ and $\lvert\eta_{det}(jet)\rvert < 1.1$ or $EmFr < 0.3$ and ($\lvert\eta_{det}(jet)\rvert < 0.1$ or $\lvert\lvert\eta_{det}(jet)\rvert - 1.15\rvert < 0.05$)

Table 8: Summary of the $\not\!\!E_T$ cleanup cuts. Note N_{twr} is the number of calorimeter towers in the jet and N_{trk} is the number of tracks associated with the jet.

After all cuts our preselection sample consists of 38,053 events left after all the quality, ID and cleanup cuts are applied. Table 9 gives a summary of the event reduction.

Requirements	Signal sample (events passed)
Trigger, Goodrun, and Standard photon ID with $\|\eta\| < 1.1$ and $E_T > 13$ GeV	45,275
Phoenix rejection	41,418
PMT spike rejection	41,412
Vertex requirements	41,402
$E_T^{swap} > 13$ GeV after vertex swap	39,719
Beam Halo rejection	39,713
Cosmic rejection (EMTiming cut)	39,663
$\not\!\!E_T$ cleanup cuts	38,053

Table 9: Summary of the $\gamma\gamma + \not\!\!E_T$ presample selection requirements and the event sample reduction. The trigger requirements are given in Table 3, the photon ID and isolation, Phoenix and PMT requirements are described in Table 4, the vertex requirements and vertex swap are described in Table 5, the beam halo rejection requirements are described in Table 6, the cosmic rejection requirements are given in Table 7 and the $\not\!\!E_T$ cleanup cuts are given in Table 8.

3 Backgrounds

3.1 Overview

The final signal region for this analysis is defined by the subsample of preselection events that also pass a set of optimized final kinematic cuts. The methods for determining the number of expected background events in the signal region are based on a combination of data and MC and allow for a large variety of potential final sets of cuts. We use these estimates as part of the optimization procedure described in Section 6. In this section we describe the backgrounds and the methods used to estimate the background rates and their uncertainties.

There are three major sources of background for $\not\!\!E_T$ in $\gamma\gamma$ candidate events. They are:

- QCD events with fake $\not\!\!E_T$:
  a) true $\gamma\gamma$, $\gamma - jet \rightarrow \gamma\gamma_{fake}$, and $jet - jet \rightarrow \gamma_{fake}\gamma_{fake}$ events where $\not\!\!E_T$ arises due to normal resolution variations in the energy measurements in the calorimeter; b) large fake $\not\!\!E_T$ due to event reconstruction pathologies such as tri-photon events with a lost photon that creates the fake $\not\!\!E_T$.

- Electroweak events with real $\not\!\!E_T$:
  a) Leptonic channel decays of a) $W\gamma\gamma$ and $Z\gamma\gamma$ events where both photons are real; b) $W\gamma$ and $Z\gamma$ events with a fake photon; c) W and Z events where both photon candidates are fake photons; d) $t\bar{t}$ production and decay.
  b) neutral leptonic channels: $Z\gamma\gamma \rightarrow \nu\bar{\nu}\gamma\gamma$, $Z\gamma \rightarrow \nu\bar{\nu}\gamma + \gamma_{fake}$ or $Z \rightarrow \nu\bar{\nu} + \gamma_{fake}\gamma_{fake}$.

- Non-collision events:
  a) PMT spikes; b) cosmic ray; c) beam-halo events where one or more of the photons and $\not\!\!E_T$ are not related to the collision.

We next discuss each in more detail, how it is estimated and how the uncertainties are calculated.

3.2 QCD Backgrounds with Fake $\not\!\!E_T$

Here we describe the QCD backgrounds and the techniques used to predict the number of expected events in the signal region after all kinematic requirements. These backgrounds come in two different categories; fake $\not\!\!E_T$ due to energy measurement fluctuations in the calorimeter as estimated using our *Met Model* ($\mathrm{N}^{\mathrm{MetModel}}_{\mathrm{signal}}$), and fake $\not\!\!E_T$ due to pathologies ($\mathrm{N}^{\mathrm{PATH}}_{\mathrm{signal}}$) such as picking the wrong vertex in events where the true collision did not create a vertex or tri-photon events with a lost photon. The total QCD background prediction in the signal region, $\mathrm{N}^{\mathrm{QCD}}_{\mathrm{signal}}$ is given by

$$\mathrm{N}^{\mathrm{QCD}}_{\mathrm{signal}} = \mathrm{N}^{\mathrm{MetModel}}_{\mathrm{signal}} + \mathrm{N}^{\mathrm{PATH}}_{\mathrm{signal}} \tag{2}$$

3.2.1 Backgrounds due to Energy Measurement Fluctuations in the Calorimeter

Standard Model QCD events, $\gamma\gamma$, $\gamma - jet \rightarrow \gamma\gamma_{fake}$, and $jet - jet \rightarrow \gamma_{fake}\gamma_{fake}$, are the dominant sources of events in the diphoton presample and a major background for $\gamma\gamma + \not\!\!E_T$. The energy measurement fluctuations in the calorimeter, which can lead to considerable values of fake $\not\!\!E_T$, happen only in a small fraction of cases, but large cross sections for these processes make them one of the largest backgrounds. We have found that rather than measure $\not\!\!E_T$, we can better reduce the QCD background by selecting events based on their $\not\!\!E_T$ *Significance* (MetSig), using a new *Met Resolution Model* [21].

The *Met Resolution Model* considers the clustered and unclustered energy in the event and calculates a probability, $P(\not\!\!E_T^{fluct} > \not\!\!E_T)$, for fluctuations in the energy measurement to produce $\not\!\!E_T^{fluct}$ equivalent to or larger than the measured $\not\!\!E_T$. This probability is then used to define a MetSig as $-\log_{10}\left(P_{\not E_T^{fluct} > \not E_T}\right)$. Events with true and fake $\not\!\!E_T$ of the same value should have, on average, different MetSig. Thus, if we suppose our data sample has $\mathrm{N_{events}}$ events which have no intrinsic $\not\!\!E_T$ then the *true* (perfect) MetSig distribution due to energy measurement fluctuations will be given by

$$\frac{dN}{dx} = \mathrm{N_{event}} \cdot ln(10) \cdot 10^{-x} \tag{3}$$

where x =MetSig. By construction a MetSig cut of 2, 3, and 4 allows ∼1.0%, ∼0.1%, and ∼0.01% of QCD events respectively[2].

This model assumes only two sources of mis-measurements that cause fake $\not\!\!E_T$. Mis-measurements from 1) jet energy clusters (jets) and 2) soft, unclustered energy (underlying event or multiple interactions). Individual contributions of each of these components to $\not\!\!E_T$ are modeled according to their energy resolution functions [21]. Jets are collimated sprays of energetic particles in a certain direction and can cause significant $\not\!\!E_T$. The unclustered energy tends to be small and uniformly spread in the calorimeter, making the portion of $\not\!\!E_T$ due to this source is usually small.

We predict $\mathrm{N_{signal}^{MetModel}}$, the QCD contribution of the background with fake $\not\!\!E_T$ that passes the kinematic cuts due to normal measurement variations, using the data. To estimate the expected MetSig for a data sample (the number of events above a given MetSig cut after the other kinematic cuts), we consider the jets and unclustered energy for each event in the sample that pass the other kinematic cuts. For each data event we throw 10 pseudo-experiments to generate a $\not\!\!E_T$ and calculate its significance, according to the jets and underlying event configuration. Then we count the number of events, $\mathrm{N_{signal}^{pseudo}}$, in the pseudo-experiments that pass our MetSig and other kinematic cuts. This number, divided by the number of pseudo-experiments, $\mathrm{N_{pseudo}} = 10$, gives us $\mathrm{N_{signal}^{MetModel}}$. In this way we can predict the MetSig distribution for lots of kinematic requirement combinations. The expected $\not\!\!E_T$ and MetSig distributions of QCD are shown in Figure 4 for the presample.

The systematic uncertainty on the number of events above a MetSig cut is evaluated by comparing the *Met Model* predictions with the default set of model parameters to predictions

[2]We will use this equation to calculate the estimated rate of events in our final sample due to energy measurement pathologies in Section 3.2.2.

obtained with the parameters deviated by $\pm\sigma$. The total uncertainty is estimated by adding the statistical uncertainty on the number of pseudo-experiments passing the cuts and adding these systematic uncertainties in quadrature.

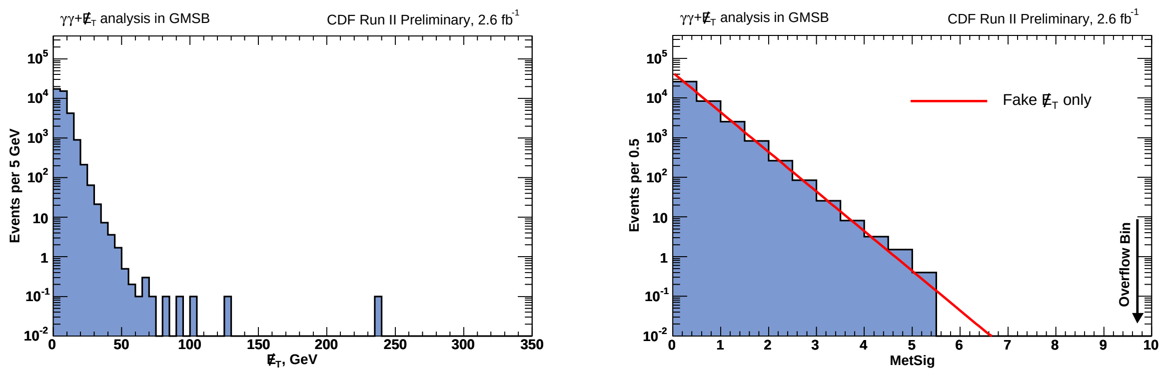

(a) (b)

Figure 4: The QCD background predictions of $\not\!\!E_T$ and MetSig using the *Met Model* for the presample. The red solid line in (b) shows the perfect prediction of fake $\not\!\!E_T$ from energy measurement fluctuations only having no instrinsic $\not\!\!E_T$. In this case, the perfect prediction of MetSig has a simple *a priori* distribution of $dN/dx = N_{event} \times ln(10) \times 10^{-x}$.

3.2.2 Backgrounds due to Event Reconstruction Pathologies

A source of QCD background that is unaccounted for by the *Met Model* is diphoton events with event reconstruction pathologies. For example, a wrong choice of the primary interaction vertex where a $\gamma\gamma$ pair is produced by one interaction and a pair of jets is produced at another vertex and produces the highest $\sum P_T$ vertex. The wrong vertex results in a $\not\!\!E_T$ mis-measurement which can be significant. As described in Section 2.2, this effect can usually be fixed by the vertex re-assignment procedure. However, there are situations when the vertex swap procedure cannot identify large fake $\not\!\!E_T$. This happens when the $\gamma\gamma$ interaction does not produce a reconstructed vertex at all, for example where $|Z_{vx}| > 60\ cm$. The *Met Model* will not be able to account for this background since this effect is not due to an energy measurement fluctuation.

A second example of QCD events whose contribution to the $\gamma\gamma + \not\!\!E_T$ signature is not estimated by the *Met Model* are events with three photon candiates but one is lost in the calorimeter. The cross section of this process is very small. However, the probability to lose a photon in the calorimeter cracks is on the order of ∼10% or more[3], so that the probability to lose one of the photon candidates in a potential tri-photon event can be ∼30% or larger.

To obtain the prediction for all events reconstruction pathologies from QCD sources at the same time, we model $\gamma\gamma$ kinematics and event reconstruction using a PYTHIA $\gamma\gamma$ sample, "cdfpstn:gx0s1g", with large statistics, and normalize to the number of events in the presample to take into account $\gamma - jet$ and $jet - jet$ contributions. Then we subtract off the

[3]This is an educated guess based on a fact that the CEM ϕ-cracks alone account for ∼8% of the CEM area. This number is not used in the analysis, rather it is just given as a value that indicates to the reader the magnitude that this is an important background.

expectations for energy mismeasurement fluctuations in the MC to avoid double counting. The final prediction of these QCD backgrounds is given by

$$\mathrm{N}_{\mathrm{signal}}^{\mathrm{PATH}} = (\mathrm{N}_{\mathrm{signal}}^{\mathrm{PATH-MC}} - \mathrm{N}_{\mathrm{signal}}^{\mathrm{MM-MC}}) \cdot \mathrm{SF}_{\mathrm{QCD}} \tag{4}$$

where $\mathrm{N}_{\mathrm{signal}}^{\mathrm{PATH-MC}}$ is the number of reconstructed PYTHIA $\gamma\gamma$ events that pass the kinematic cuts (including the MetSig cut), $\mathrm{N}_{\mathrm{signal}}^{\mathrm{MM-MC}}$ is the estimated rate of energy measurement fluctuation events passing the final kinematic cuts, and $\mathrm{SF}_{\mathrm{QCD}}$ is a scale factor to normalize the MC sample to the data and take into account the fact that the MC has only $\gamma\gamma$ events, whereas QCD backgrounds come from $\gamma\gamma$, $\gamma - jet$, or $jet - jet$ sources; the pathologies should be similar. The estimated rate of energy measurement fluctuation events passing the final cuts is given by

$$\mathrm{N}_{\mathrm{signal}}^{\mathrm{MM-MC}} = \mathrm{N}_{\mathrm{signal}}^{\mathrm{noMetSig\ cut}} \cdot \mathrm{R}_{\mathrm{MetSig}}^{\mathrm{exp}} \tag{5}$$

where $\mathrm{N}_{\mathrm{signal}}^{\mathrm{noMetSig\ cut}}$ is the number of events in the MC that pass all the kinematic cuts except the MetSig cut, and $\mathrm{R}_{\mathrm{MetSig}}^{\mathrm{exp}}$ is the expected rate for events to pass the MetSig cut using Eq.(2). The scale factor, $\mathrm{SF}_{\mathrm{QCD}}$, is taken to be equal to the number of events passing the preselection cuts in data (the presample is dominated by QCD) and in the MC sample. The number of events that pass the preselection cuts for data ($\mathrm{N}_{\mathrm{presample}}^{\mathrm{QCD-Data}}$) and MC ($\mathrm{N}_{\mathrm{presample}}^{\mathrm{QCD-MC}}$) are 38,053 and 283,554 respectively. We find

$$\mathrm{SF}_{\mathrm{QCD}} = \frac{\mathrm{N}_{\mathrm{presample}}^{\mathrm{QCD-Data}}}{\mathrm{N}_{\mathrm{presample}}^{\mathrm{QCD-MC}}} = \frac{38,053}{283,554} = 0.134 \pm 0.007 \quad (\mathrm{stat.only}). \tag{6}$$

The expected $\not\!\!E_T$, MetSig, H_T and $\Delta\phi(\gamma_1, \gamma_2)$ distributions for the $\gamma\gamma$ MC sample passing the preselection cuts are shown in Figure 5. The tails in Figure 5-(b) for the MetSig are long and, as expected, are dominated by tri-photon and wrong vertex events.

The systematic uncertainties on this background prediction include the uncertainty on the scale factor and the uncertainty due to MC-data differences in the unclustered energy parameterization and the jet energy scale. To get the systematic uncertainty on the unclustered energy parametrization from the *Met Model* we deviate the default set of parameters by $\pm\sigma$. For the systematic uncertainty on the jet energy scale we follow the standard procedure at CDF [34]. An additional systematic uncertainty due to the fact that the presample isn't pure QCD (see, for example, Figure 12), is overestimated to be 5% and is taken in quadrature. The total uncertainty is estimated by adding the statistical uncertainty and these systematic uncertainties in quadrature.

After estimating all classes of QCD backgrounds, the expected kinematic distributions for the combined QCD sources, after the preselection requirements, are shown in Figure 6.

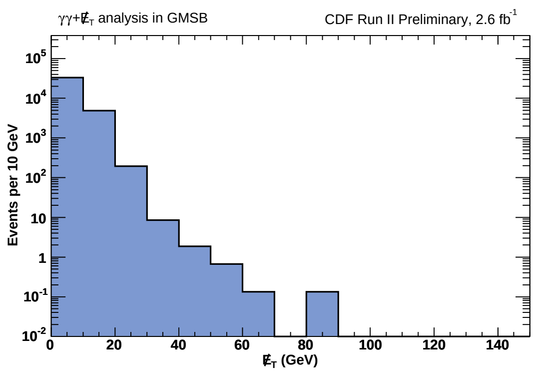

(a)

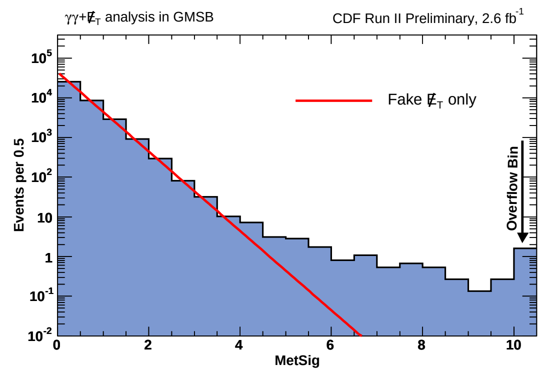

(b)

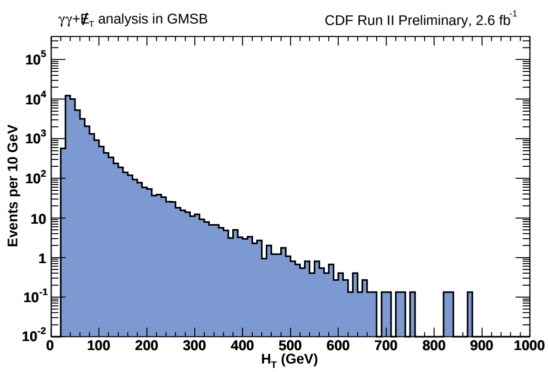

(c)

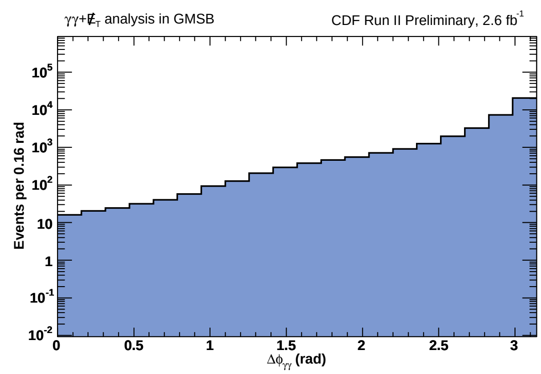

(d)

Figure 5: The $\not\!\!E_T$, MetSig, H_T, and $\Delta\phi(\gamma_1, \gamma_2)$ distributions for the PYTHIA $\gamma\gamma$ MC sample after the preselection requirements, but normalized by the $\mathrm{SF_{QCD}}$ scale factor. The tails in the MetSig are long, but the overall rate of this process is low.

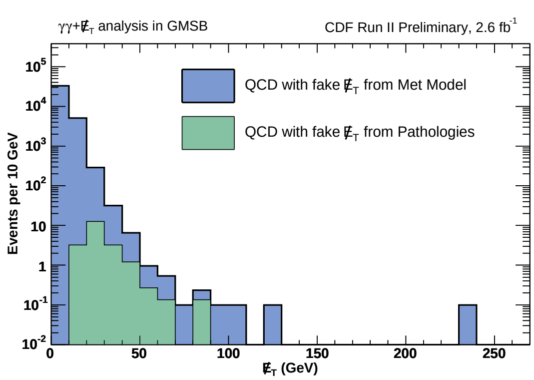

(a)

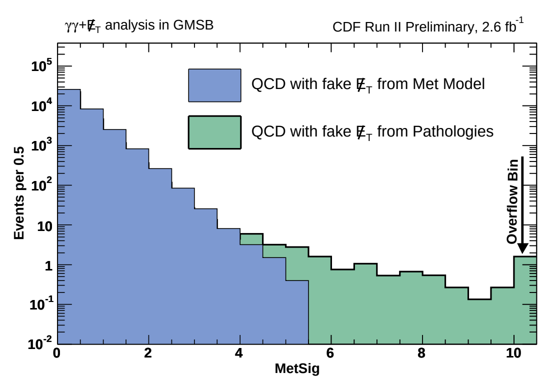

(b)

Figure 6: The combined QCD background predictions after the preselection requirements. (a) and (b) show $\not\!\!E_T$ and MetSig distributions respectively.

3.3 Electroweak Backgrounds with Real $\not\!\!E_T$

Electroweak processes involving W's and Z's are the most common source of real and significant $\not\!\!E_T$ in $p\bar{p}$ collisions. We estimate the background rate from decays into both charged and neutral leptons.

There are four ways we can get a $\gamma\gamma + \not\!\!E_T$ signature in electroweak events: 1) from $W\gamma\gamma$ and $Z\gamma\gamma$ events where both photons are real; 2) from $W\gamma$ and $Z\gamma$ events with a fake photon; 3) from W and Z events where both photon candidates are fake photons; and 4) $t\bar{t}$ production and decay. As we will see, out of these sources $Z\gamma + jet \rightarrow \nu\nu\gamma + \gamma_{fake}$ events are the dominant electroweak background in our analysis after all kinematic requirements.

To estimate the contribution from the electroweak backgrounds we mostly use the standard electroweak MC samples [35], according to their production cross section and k-factors, but normalized to data. The Baur $W\gamma$ and $Z\gamma$ samples are used to evaluate contributions from both $W/Z + \gamma$ and $W/Z + \gamma\gamma$ events using ISR/FSR in the charged deacy modes. The inclusive PYTHIA W and Z samples are used to obtain the contribution from $W + jet$ and $Z + jet$ events where both photon candidates are fakes and $t\bar{t}$ events. Also we use a custom inclusive PYTHIA $Z(\nu\bar{\nu})\gamma$ to estimate contributions from neutral leptonic decays. We consider here all leptonic decay modes of W and Z bosons. To avoid overlaps between Baur and PYTHIA, we filter out PYTHIA events where photons reconstructed in the detector are matched to HEPG level photons from either quark ISR or lepton FSR.

The electroweak background predictions are given by

$$\mathrm{N}^{\mathrm{EWK}}_{\mathrm{signal}} = \sum_{i=0}^{n} \mathrm{N}^{\mathrm{EWK-MC}}_{\mathrm{signal},i} \cdot \mathrm{SF}_i \cdot \left(\frac{\mathrm{N}^{\mathrm{Data}}_{e\gamma,\mathrm{signal}}}{\mathrm{N}^{\mathrm{MC}}_{e\gamma,\mathrm{signal}}} \right) \tag{7}$$

where $\mathrm{N}^{\mathrm{EWK-MC}}_{\mathrm{signal},i}$ is the number of events passing all the final kinematic cuts from MC sample i, for each electroweak source. The scale factors, SF_i, normalizes each electroweak background to its production cross section and k-factor. To minimize the dependence of our predictions for potential Data-MC differences (trigger efficiencies, acceptance and ID efficiencies, modeling of ISR/FSR, PDF uncertainties, luminosity uncertainties, etc.), we normalize, using the rate of the number of $e\gamma$ events observed in the data that also pass all signal kinematic cuts, $\mathrm{N}^{\mathrm{Data}}_{e\gamma,\mathrm{signal}}$, to the number of events observed in MC's, $\mathrm{N}^{\mathrm{MC}}_{e\gamma,\mathrm{signal}}$. To minimize differences between $e\gamma$ and $\gamma\gamma$ samples, electrons are required to satisfy the photon-like ID requirements listed in Table 10. Here, and later, we will refer to the ratio of $\left(\frac{\mathrm{N}^{\mathrm{Data}}_{e\gamma,\mathrm{signal}}}{\mathrm{N}^{\mathrm{MC}}_{e\gamma,\mathrm{signal}}} \right)$ as the global electroweak normalization factor.

The scale factors are calculated using

$$\mathrm{SF}_i = \frac{\sigma_i \cdot \mathrm{k}_i \cdot \mathcal{L}}{\mathrm{N}^{\mathrm{EWK}}_{\mathrm{sample},i}} \tag{8}$$

where for each source i σ_i is production cross section, k_i is the k-factor, $\mathcal{L}$ is the 2.6 fb^{-1} of luminosity and $\mathrm{N}^{\mathrm{EWK}}_{\mathrm{sample},i}$ is the number of events in the MC sample after passing goodrun. The results are summarized in Table 11. The normalization to data term, $\mathrm{N}^{\mathrm{MC}}_{e\gamma,\mathrm{signal}}$, is calculated using

The Standard Photon-like Electron ID Cuts	
detector	CEM
Conversion*	No
corrected E_T	≥ 13 GeV
CES fiduciality	$\lvert X_{\mathrm{CES}}\rvert \leq 21$ cm 9 cm $\leq \lvert Z_{CES}\rvert \leq 230$ cm
average CES χ^2	≤ 20
Had/Em	$\leq 0.055 + 0.00045 \times E$
corrected CalIso0.4	$\leq$0.1$\times E_T$ if E_T<20 GeV or $\leq$2.0+0.02$\times(E_T - 20)$
$N3D$ tracks in cluster*	1 or 2
E/P of 1^{st} track*	0.8$\leq E/P \leq$1.2 if $P_T < 50$ GeV no cut if $P_T \geq 50$ GeV
2^{nd} track P_T if $N3D = 2$*	$\leq$1.0+0.005$\times E_T$
$TrkIso0.4 - P_T^{1^{st}trk}$	$\leq 2.0 + 0.005 \times E_T$
E_T of 2^{nd} CES cluster (wire and strip)	$\leq$0.14$\times E_T$ if E_T<18 GeV $\leq$2.4+0.01$\times E_T$ if $E_T \geq$18 GeV
$\Delta z = \lvert z_{trk} - z_{vx}\rvert$*	$\lvert\Delta z\rvert \leq 3$ cm

Table 10: The photon-like electron ID cuts used to make the $e\gamma$ data set in data and MC. Cuts that are different from the standard photon ID and isolation, given in Table 4, are indicated with a *. Also, no additional cuts in Table 4 such as PMT spikes and Phoenix rejection cuts are added.

$$\mathrm{N}^{\mathrm{MC}}_{e\gamma,\mathrm{signal}} = \sum_{i=0}^{n} \mathrm{N}^{\mathrm{MC}}_{e\gamma,\mathrm{signal},i} \cdot \mathrm{SF}_i. \tag{9}$$

The uncertainty on the electroweak backgrounds are dominated by the $e\gamma$ normalization factor uncertainty. This includes data and MC statistical uncertainties as well as differences in MC modeling. The last uncertainty is estimated by comparing results for a default value of the E/p cut ($0.8 < E/p < 1.2$) and a deviated value of the E/p cut ($E/p < 2.0$) for variation of scale factor as a function of the cuts. As we will see this is comparable to the variation of the overall scale factor as the final kinematic requirements are varied. The total uncertainties also include the MC statistical uncertianties and uncertainties on the normalization factors added in quadrature.

The expected $\not\!\!E_T$, MetSig, H_T and $\Delta\phi(\gamma_1, \gamma_2)$ distributions for the electroweak backgrounds in the presample are shown in Figure 7.

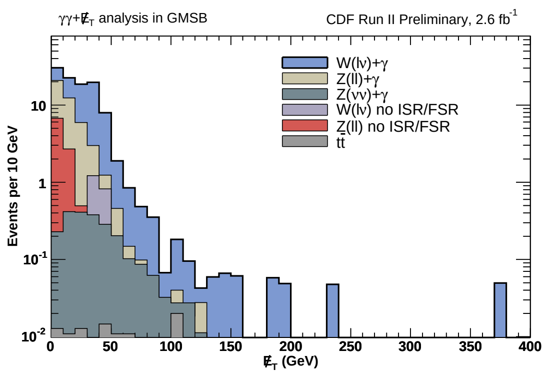

(a)

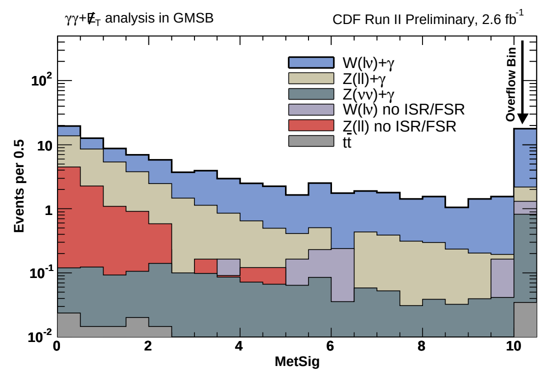

(b)

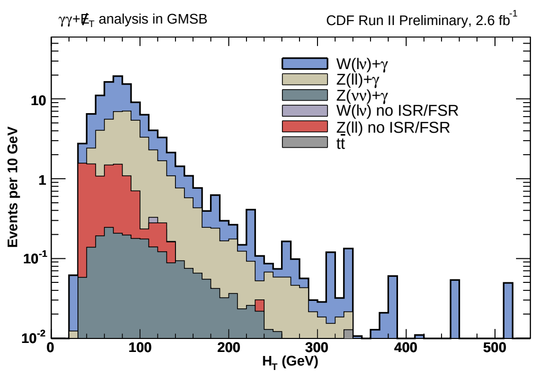

(c)

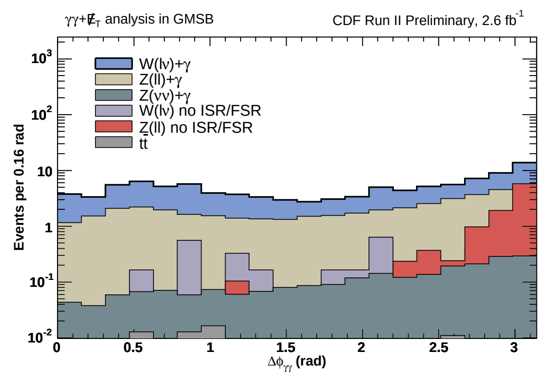

(d)

Figure 7: The electroweak background predictions after the preselection requirements. (a), (b), (c), and (d) show the $\not\!\!E_T$, MetSig, H_T, and $\Delta\phi(\gamma_1, \gamma_2)$ distributions respectively. The global scale factor for the preselection cuts, 0.78, is used.

Background Source	Cross Section σ_i(pb)	k-factor k_i	MC events $N^{EWK}_{sample,i}$	MC-to-Data SF SF_i
$W(e\nu)+\gamma$	32.0	1.36	1,775,122	0.0635
$W(\mu\nu)+\gamma$	32.0	1.34	1,836,273	0.0605
$W(\tau\nu)+\gamma$	32.0	1.34	1,824,182	0.0609
$Z(ee)+\gamma$	10.3	1.36	9,258,132	0.0039
$Z(\mu\mu)+\gamma$	10.3	1.36	9,214,135	0.0040
$Z(\tau\mu)+\gamma$	10.3	1.36	9,196,501	0.0040
$Z(\nu\bar{\nu})+\gamma$	2.5	1.4	8,766,307	0.0010
$W(e\nu)$ no ISR/FSR	1,960	1.4	33,815,147	0.210
$W(\mu\nu)$ no ISR/FSR	1,960	1.4	23,058,663 (10,166,426)	0.308 (0.699)
$W(\tau\nu)$ no ISR/FSR	1,960	1.4	24,057,340	0.296
$Z(ee)$ no ISR/FSR	355	1.4	22,986,333	0.056
$Z(\mu\mu)$ no ISR/FSR	355	1.4	14,704,660 (10,203,233)	0.0876 (0.126)
$Z(\tau\tau)$ no ISR/FSR	355	1.4	33,278,066	0.0387
$t\bar{t}$ (incl.)	6.7	N/A	7,430,826	0.0023

Table 11: Scale factors for the individual electroweak backgrounds. Note that the scale factors for $W(\mu)$ no ISR/FSR and $Z(\mu)$ no ISR/FSR are listed twice. For these two samples only parts of the samples were used in the $e\gamma$ counting experiment as they are low rate processes. Note also that we use the $E_T > 7$ GeV and $|\eta| < 1.5$ requirements to generate $Z(\nu\bar{\nu}) + \gamma$ sample.

3.4 Non-Collision Events

Non-collision backgrounds to the $\gamma\gamma + \not\!\!E_T$ background come from PMT spikes, beam halo (B.H.) and cosmic rays (C.R.) sources where either a single or double photon-like signature comes from the non-collision source. Because these events do not originate from beam-beam interactions, they can be a source of significant spurious $\not\!\!E_T$. It was shown in Ref. [25] that other sources of spurious energy in $\gamma\gamma$ events are negligible.

PMT spikes, while not rare, do have a distinct signature (see Ref. [31]) and our PMT asymmetry requirement removes them very efficiently. Therefore, we do not explicitly evaluate this background and take the number of remaining PMT spikes backgrounds events to be zero. We next discuss beam halo and cosmic rays.

3.4.1 Beam Halo Events

As discussed in Ref. [31] B.H. events fake the $\gamma\gamma + \not\!\!E_T$ final state when high energy muons, produced in beam-beam pipe interactions, interact with the calorimeter and fake two photons. For geometric reasons these photon candidates are typically located in the same wedge, mostly wedges 0 and 23. Single γ B.H. overlapping a SM γ event, as previously mentioned, is taken to be negligible [21].

To estimate the B.H. contribution to the $\gamma\gamma + \not\!\!E_T$ final state after the B.H. rejection procedure described in Section 2.2, we use a loose beam halo enriched $\gamma\gamma$ sample. These events are used to predict the shape of the kinematic distributions as well as their correlations. To predict the expected number of B.H. events after all final cuts we then correct this sample for differences in the requirements between the loose cut sample and the final signal sample. The B.H. enriched sample is selected as having two loose photon candidates passing the requirements of Table 12, and identified as a beam halo using the cuts in Table 6. To increase the statistics we do not require a vertex, nor do we reject events that fail the EMTiming requirements. We will correct for these also. A total of 13 events, $\mathrm{N}^{\mathrm{BH}}_{\mathrm{control}}$, make up this sample. We use all 13 events as a template for the kinematic distributions, as shown in Figure 8

To take this sample to the prediction of the number of events in the signal region we multiply by the measured rate at which these events pass the kinematic cuts as well as the rate they pass the ID and isolation, vertex and timing cuts. Finally we take into account the efficiency for B.H. events to be in this sample. Using these pieces we calculate the final rate as follows:

$$\mathrm{N}^{\mathrm{BH}}_{\mathrm{signal}} = \mathrm{N}^{\mathrm{BH}}_{\mathrm{control}} \cdot \mathrm{R}^{\mathrm{BH}}_{\mathrm{ID,VX,T}} \cdot \mathrm{R}^{\mathrm{BH}}_{\mathrm{kinematic}} \cdot \frac{1}{\epsilon_{\mathrm{BH}}} \tag{10}$$

where $\mathrm{R}^{\mathrm{BH}}_{\mathrm{ID,VX,T}}$ is the rejection factor that takes into account the power of the photon ID and isolation, vertex and timing cuts, $\mathrm{R}^{\mathrm{BH}}_{\mathrm{kinematic}}$ is the rejection factor that estimates the rate at which B.H. events pass the kinematic requirements, and $\frac{1}{\epsilon_{\mathrm{BH}}}$ takes into account the fraction of B.H. events that are not in our sample. The first rejection factor, $\mathrm{R}^{\mathrm{BH}}_{\mathrm{ID,VX,T}}$, is estimated by

$$\mathrm{R}^{\mathrm{BH}}_{\mathrm{ID,VX,T}} = \frac{\mathrm{N}^{\mathrm{BH-control}}_{\mathrm{ID,VX,T}}}{\mathrm{N}^{\mathrm{BH}}_{\mathrm{control}}} = \frac{1}{13} \tag{11}$$

where $N^{BH-control}_{ID,VX,T} = 1$ is the number of events in the control sample that also pass the photon ID and isolation requirements, vertex requirements and the EMTiming cuts. The $R^{BH}_{kinematic}$, rejection factor for the final kinematic cuts is estimated by

$$R^{BH}_{kinematic} = \frac{N^{BH-control}_{kinematic}}{N^{BH}_{control}} = \frac{N^{BH-control}_{kinematic}}{13} \tag{12}$$

where $N^{BH-control}_{kinematic}$ is the number of events in the control sample that also pass the final kinematic cuts described in Section 6. To normalize to the lost rate of B.H. events in our sample we take

$$\frac{1}{\epsilon_{BH}} = \frac{(1 - R_{BH})}{R_{BH}} = \frac{1 - 0.9}{0.9} = 0.11 \tag{13}$$

where we have used $R_{BH} = 0.9 = 90\%$ as the rejection power, taken from Ref. [21], since the B.H. ID requirements are 90% efficient in identifying B.H. events. Thus, the final expected number of B.H. events in the signal region that pass the final kinematic cuts is given by

$$\begin{aligned} N^{BH}_{signal} &= N^{BH}_{control} \cdot R^{BH}_{ID,VX,T} \cdot R^{BH}_{kinematic} \cdot \frac{1}{\epsilon_{BH}} \\ &= 13 \cdot \frac{1}{13} \cdot \frac{N^{BH-control}_{kinematic}}{13} \cdot 0.11 \\ &= N^{BH-control}_{kinematic} \cdot (0.008) \\ &= N^{BH-control}_{kinematic} \cdot SF_{BH} \end{aligned} \tag{14}$$

where we take $SF_{BH} = 0.008 \pm 0.008$ (stat. only).

The uncertainty on the B.H estimation is dominated by the statistical uncertainty on the number of events after all kinematic cuts in the B.H. control sample, $N^{BH-control}_{kinematic}$. The other major source of uncertainty is the uncertainty on fraction of B.H. events that pass the vertex, ID and EMTiming cuts.

Cuts	Loose photon control sample ID
detector	CEM
corrected E_T	$\geq$ 13 GeV
CES fiduciality	$\lvert X_{\rm CES}\rvert \leq 21$ cm 9 cm $\leq \lvert Z_{CES}\rvert \leq 230$ cm
average CES χ^2	$\leq$20
Had/Em*	$\leq$0.125
corrected CalIso0.4*	$\leq 0.15\times E_T$ if E_T<20 GeV or $\leq 3.0+0.02\times(E_T-20)$
TrkIso0.4	≤ 5
$N3D$ tracks in cluster*	≤ 1
track P_T if $N3D = 0$*	$\leq 0.25\times E_T$
E_T of 2^{nd} CES* cluster (wire and strip)	no cut

Table 12: Summary of the standard loose photon ID cuts used to create our non-collision enriched background samples. Cuts that are different from the standard photon ID and isolation requirements, without the two additional requirements, PMT and Phoenix cuts, given in Table 4, are indicated with a *.

Passing one of the triggers in Table 3
Two photons passing the loose photon ID cuts in Table 12
No vertex requirements
$\lvert T_{\gamma_1}\rvert$ or $\lvert T_{\gamma_2}\rvert < 20$ ns
Two photons identified by the Beam Halo ID cuts listed in Table 6
$\not\!\!E_T$ >20 GeV

Table 13: Summary of cuts used to select the beam halo enriched sample. A total of 13 events pass these requirements.

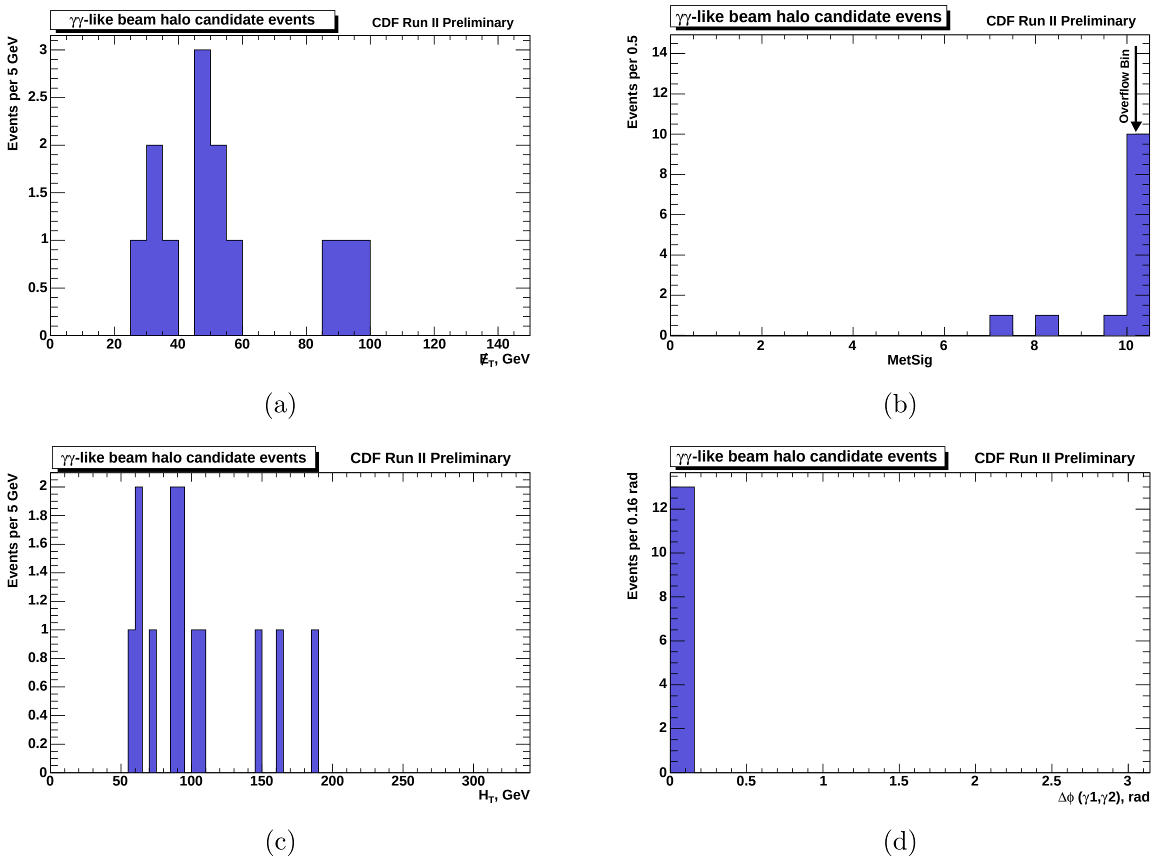

Figure 8: The $\not\!\!E_T$, MetSig, H_T and $\Delta\phi(\gamma_1, \gamma_2)$ distributions for the 13 events in the $\gamma\gamma$ beam-halo enriched sample. Events are selected using the requirements in Table 13. As expected these events have large MetSig. They have small $\Delta\phi(\gamma_1, \gamma_2)$ by construction.

3.4.2 Cosmic Ray Events

Cosmic ray (C.R.) muon events fake the $\gamma\gamma + \not\!\!E_T$ signature via photon bremsstrahlung as the muon traverses the magnet, or by catastrophic interaction with the EM calorimeter. In addition to using the EMTiming system to remove contamination due to cosmic rays (see Table 7), we also use it, and similar techniques as above, to evaluate the remaining contribution after the kinematic cuts. We select a cosmic ray enriched sample of $\gamma\gamma + \not\!\!E_T$ candidate events by selecting events with two photons passing the loose photon ID cuts in Table 12, but failing the timing cuts. Specifically, at least one of the photon candidate must have $\mathrm{T}_\gamma > 25$ ns. That way we take into account all cosmic ray sources; both photons from the same cosmic ray, each photons from a different cosmic ray, and one photon where comes from a cosmic ray and one from the collision. To increase the sample statistics events are not required to pass our vertex cut, which we correct for in our sample estimate. The full set of requirements are given in Table 14. This gives us a pure sample of 40 C.R. events, $\mathrm{N}^{\mathrm{CR}}_{\mathrm{control}}$. We use all 40 events as a template for the $\not\!\!E_T$, MetSig, H_T and $\Delta\phi(\gamma_1, \gamma_2)$ distributions, as shown in Figure 9, from which we will get the kinematic rejection fraction, $\mathrm{R}^{\mathrm{CR}}_{\mathrm{kinematic}}$.

Passing one of the triggers in Table 3
Two photons passing the loose photon ID cuts in Table 12
No vertex requirements
$\lvert T_{\gamma_1}\rvert$ or $\lvert T_{\gamma_2}\rvert > 25$ ns

Table 14: Summary of cuts used to select the cosmic ray enriched sample. A total of 40 events pass these requirements.

To estimate the expected number of C.R. events in the signal region, we take

$$\mathrm{N}^{\mathrm{CR}}_{\mathrm{signal}} = \mathrm{N}^{\mathrm{CR}}_{\mathrm{control}} \cdot \mathrm{R}^{\mathrm{CR}}_{\mathrm{kinematic}} \cdot \mathrm{R}^{\mathrm{CR-window[25,120]}}_{\mathrm{ID,VX}} \cdot \mathrm{R}^{\mathrm{CR}}_{\Delta\mathrm{T}} \tag{15}$$

where $\mathrm{R}^{\mathrm{CR-window[25,120]}}_{\mathrm{ID,VX}}$ is the rejection factor to estimate the rate at which C.R. events have both photons passing the photon ID cuts and the vertex requirements. This factor takes into account the extrapolation from the control timing window, [25,120] ns, into signal timing window, [$4\cdot\sigma_T$,$-4\cdot\sigma_T$] ns. The $\mathrm{R}^{\mathrm{CR}}_{\Delta\mathrm{T}}$ term is the rejection factor to estimate the rate at which C.R. events pass a cut on $\Delta\mathrm{T}_{\gamma\gamma}$ between arrival time of two photons. The first rejection factor, $\mathrm{R}^{\mathrm{CR}}_{\mathrm{kinematic}}$, is estimated by

$$\mathrm{R}^{\mathrm{CR}}_{\mathrm{kinematic}} = \frac{\mathrm{N}^{\mathrm{CR-control}}_{\mathrm{kinematic}}}{\mathrm{N}^{\mathrm{CR}}_{\mathrm{control}}} = \frac{\mathrm{N}^{\mathrm{CR-control}}_{\mathrm{kinematic}}}{40} \tag{16}$$

where $\mathrm{N}^{\mathrm{CR-control}}_{\mathrm{kinematic}}$ is the number of events in the control sample that pass the final kinematic cuts defined in Section 6. To estimate the second rejection factor, $\mathrm{R}^{\mathrm{CR-window[25,120]}}_{\mathrm{ID,VX}}$, we count the number of events in the control region timing window [25,120] ns that pass the photon ID and vertex requirements and extrapolate into the signal region timing window [$-4\cdot\sigma_T$,$4\cdot\sigma_T$] ns, where $\sigma_T = 1.665$ ns, using the observed flat timing distribution [31, 32] shown in Figure 10. The $\mathrm{R}^{\mathrm{CR-window[25,120]}}_{\mathrm{ID,VX}}$ term is estimated by

$$
\begin{aligned}
\mathrm{R}^{\mathrm{CR-window[25,120]}}_{\mathrm{ID,VX}} &= \frac{\mathrm{N}^{\mathrm{CR-window[25,120]}}_{\mathrm{ID,VX}}}{\mathrm{N}^{\mathrm{CR}}_{\mathrm{control}}} \cdot \frac{(4\cdot\sigma_T - (-4\cdot\sigma_T))\mathrm{ns}}{(120-25)\mathrm{ns}} \\
&= \frac{7}{40} \cdot \frac{(4\cdot 1.665 - (-4\cdot 1.665))\mathrm{ns}}{(120-25)\mathrm{ns}} = 0.025 \qquad (17)
\end{aligned}
$$

where $\mathrm{N}^{\mathrm{CR-window[25,120]}}_{\mathrm{ID,VX}} = 7$ is the number of events that pass the photon ID and vertex requirement where either photon has the arrival time in the range [25,120] ns. The last rejection fraction, $\mathrm{R}^{\mathrm{CR}}_{\Delta\mathrm{T}}$, for the $\Delta\mathrm{T}_{\gamma\gamma}$ cut between arrival time of two photons, is given by

$$
\mathrm{R}^{\mathrm{CR}}_{\Delta\mathrm{T}} = \frac{\mathrm{N}^{\mathrm{CR-ID,VX}}_{\Delta\mathrm{T}}}{\mathrm{N}^{\mathrm{CR}}_{\mathrm{control}}} = \frac{1}{40} \qquad (18)
$$

where $\mathrm{N}^{\mathrm{CR-ID,VX}}_{\Delta\mathrm{T}} = 1$ is the number of events that pass the photon ID and vertex cuts with $\Delta\mathrm{T}_{\gamma\gamma} < 5\cdot\sigma_{\Delta\mathrm{T}}$ ns between arrival times of both photons, where $\sigma_{\Delta\mathrm{T}} = 1.021$ ns[4]. Thus, the final expected number of C.R. events in the signal region that pass the final kinematic cuts is given by

$$
\begin{aligned}
\mathrm{N}^{\mathrm{CR}}_{\mathrm{signal}} &= \mathrm{N}^{\mathrm{CR}}_{\mathrm{control}} \cdot \mathrm{R}^{\mathrm{CR}}_{\mathrm{kinematic}} \cdot \mathrm{R}^{\mathrm{CR-window}}_{\mathrm{ID,VX}} \cdot \mathrm{R}^{\mathrm{CR}}_{\Delta\mathrm{T}} \\
&= 40 \cdot \frac{\mathrm{N}^{\mathrm{CR-control}}_{\mathrm{kinematic}}}{40} \cdot 0.025 \cdot \frac{1}{40} \\
&= \mathrm{N}^{\mathrm{CR-control}}_{\mathrm{kinematic}} \cdot (0.001) \\
&= \mathrm{N}^{\mathrm{CR-control}}_{\mathrm{kinematic}} \cdot \mathrm{SF}_{\mathrm{CR}} \qquad (19)
\end{aligned}
$$

where we take $\mathrm{SF}_{\mathrm{CR}} = 0.001 \pm 0.001$. (stat. only).

The uncertainties are dominated by statistical uncertaintiy on the number of identified cosmics events and the various subsamples.

After estimating beam halo and cosmic ray backgrounds, the expected kinematic distributions for combined non-collision backgrounds in the presample are shown in Figure 11.

[4]We used $4\cdot\sigma_{\Delta\mathrm{T}}$, but since found no events we extended it to $5\cdot\sigma_{\Delta\mathrm{T}}$ to overestimate this background.

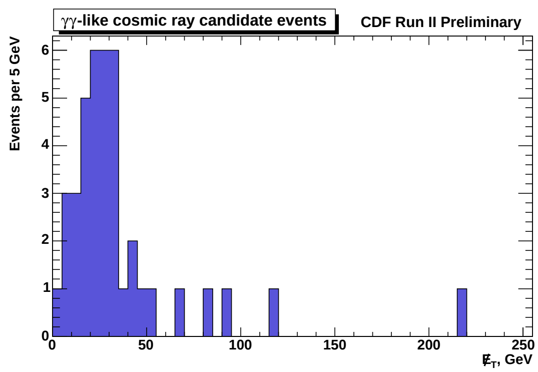

(a)

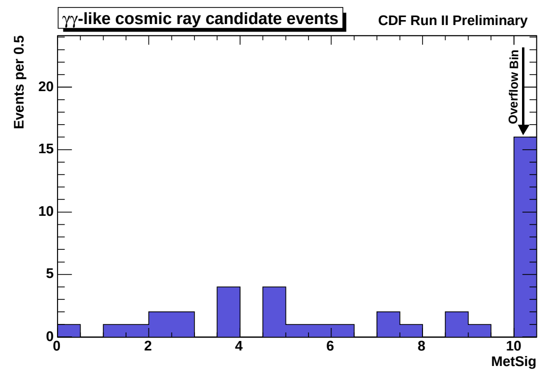

(b)

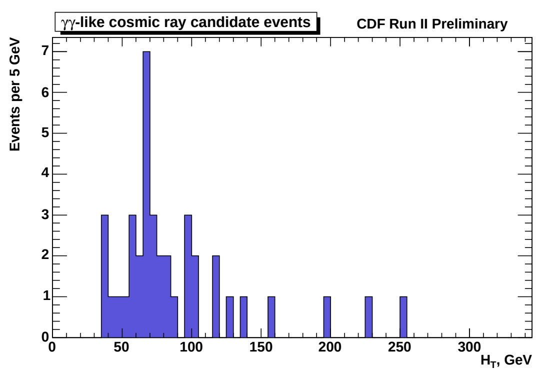

(c)

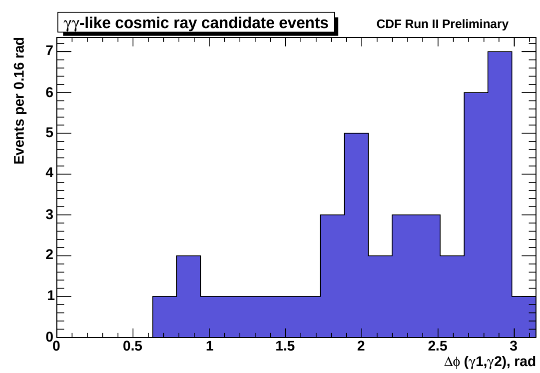

(d)

Figure 9: The $\not\!\!E_T$, MetSig, H_T and $\Delta\phi(\gamma_1, \gamma_2)$ distributions for the 40 $\gamma\gamma$ candidate events in the cosmic ray enriched sample. Events are selected using the requirements in Table 14.

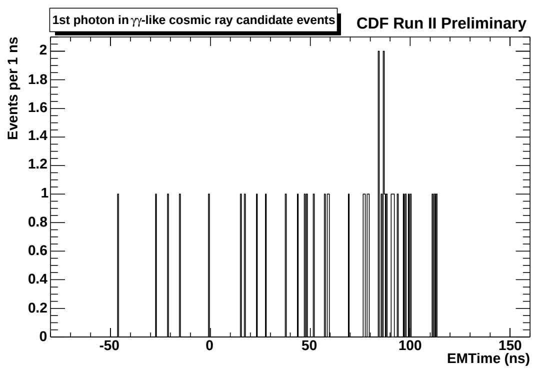

(a)

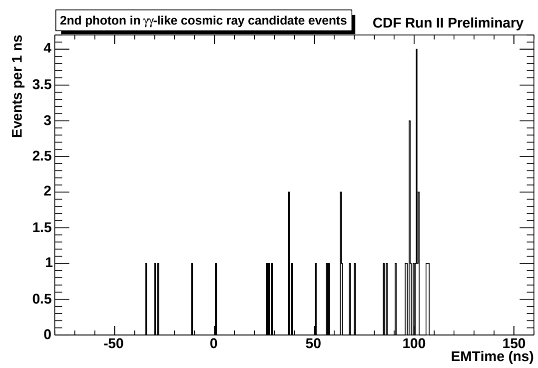

(b)

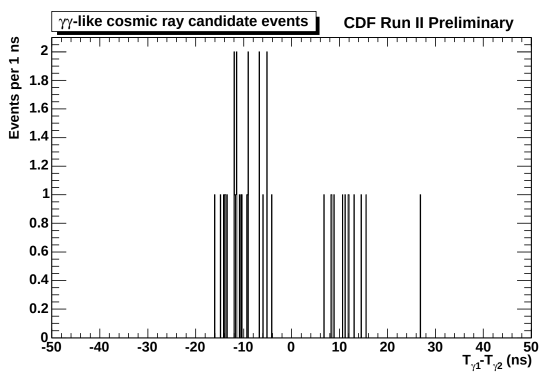

(c)

Figure 10: The EMTiming distributions for the first and second photons in (a) and (b) for the 40 observed $\gamma\gamma$-like cosmic events selected using the requirements in Table 14. Figure (c) shows the $\Delta T_{\gamma\gamma} = T_{\gamma 1} - T_{\gamma 2}$ between the arrival times of the two photons.

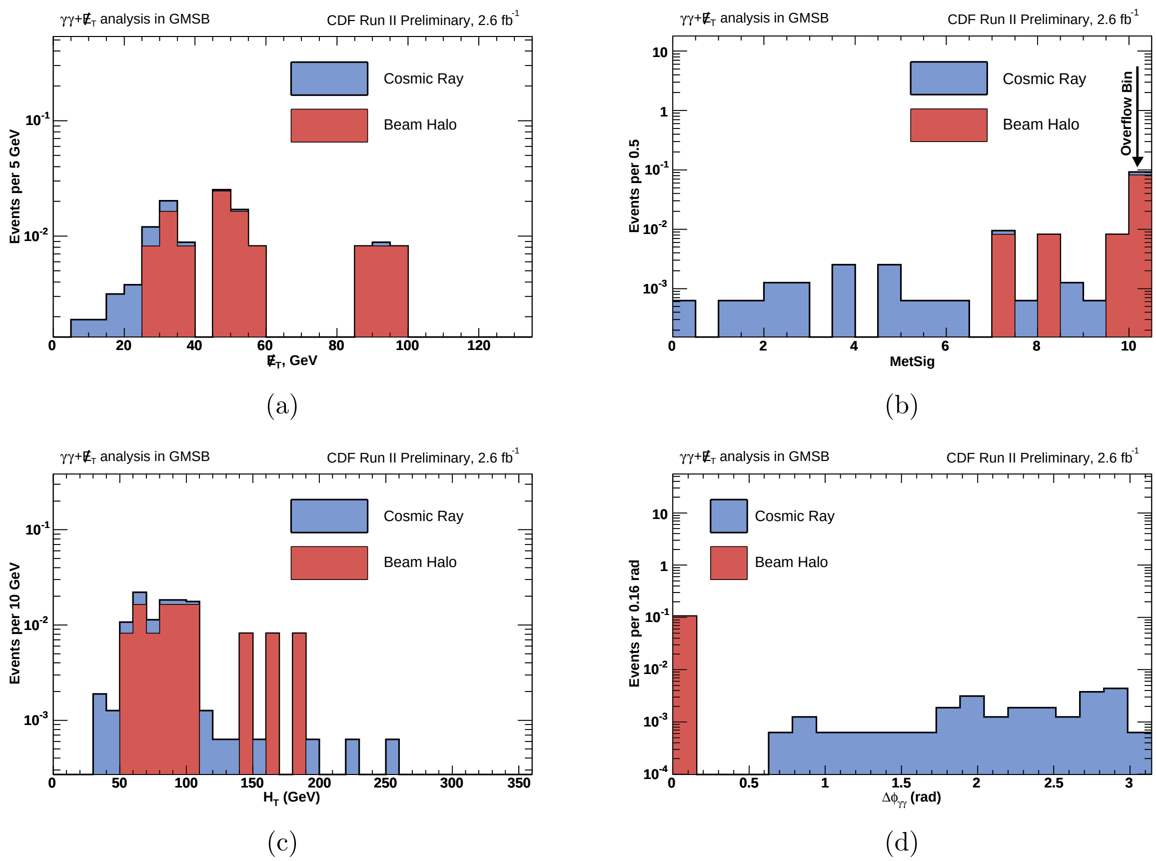

Figure 11: The non-collision background predictions after the preselection requirements, but with B.H. and C.R. normalized by $\mathrm{SF_{BH}}$ and $\mathrm{SF_{CR}}$ respectively. (a), (b), (c) and (d) show the $\not\!E_T$, MetSig, H_T and $\Delta\phi(\gamma_1, \gamma_2)$ distributions respectively.

3.5 Background Summary

After considering all the backgrounds, the expected kinematic distributions, normalized to expectations, for all combined backgrounds of QCD, electroweak and non-collision for the presample are shown in Figure 12. The MetSig in Figure (b) shows the clear separation between the QCD (99.7%) and EWK (0.3%) backgrounds showing the power of our background estimation techniques and our understanding level of the data sample. Note that events at large MetSig=10 in Figure (b) are overflow bins.

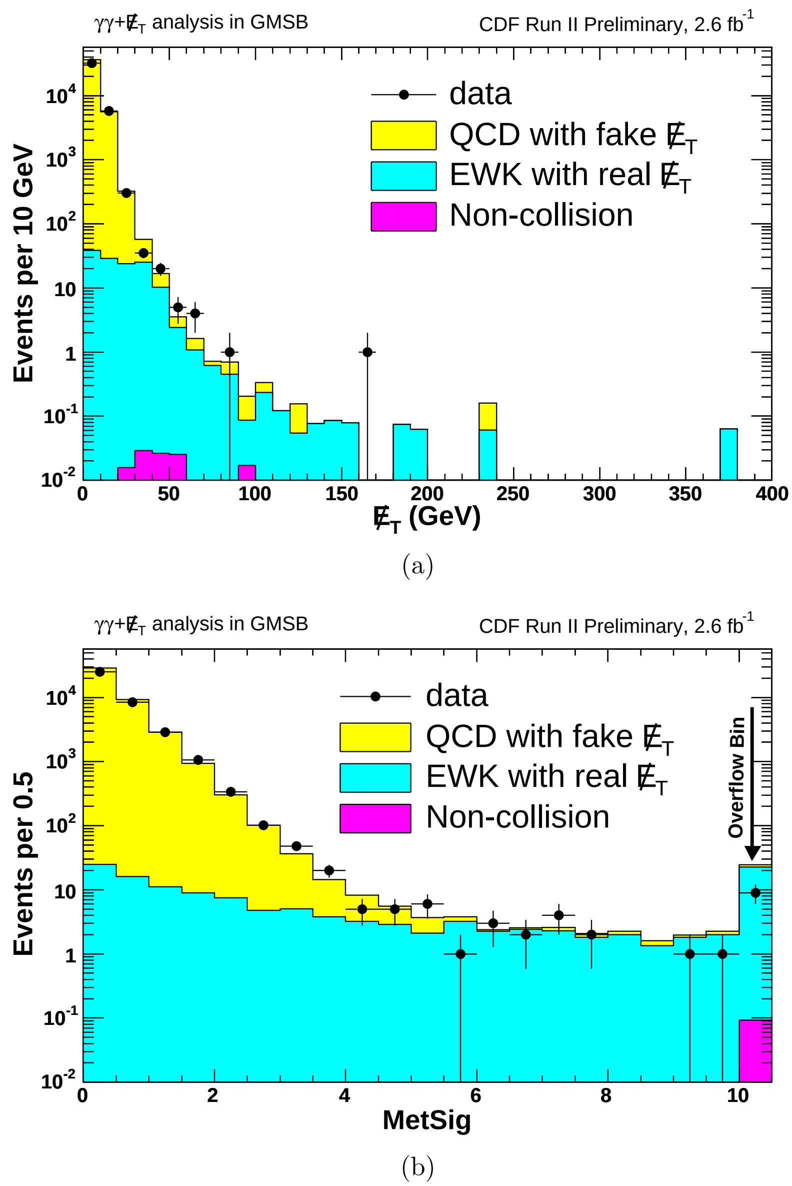

Figure 12: The $\not\!\!E_T$ and MetSig predictions after the preselection requirements along with the data.

4 Acceptances for GMSB Models

In this section we describe how we estimate our signal acceptance using an MC simulation of the GMSB model. For the purpose of this analysis we consider a GMSB model with the following parameters fixed on the minimal-GMSB Snowmass slope constraint (SPS 8) that is commonly used [16, 17]:

$$N = 1, \;\; M_m/\Lambda = 2, \;\; \tan\beta = 15, \;\; \mu > 0.$$

This reduces the six free parameters in Table 1 to two which we take as the $m_{\tilde{\chi}_1^0}$ and $\tau_{\tilde{\chi}_1^0}$. To simulate events we use the PYTHIA event generator and use *cdfSim* of *cdfsoft* release 6.1.4 [11, 36] with the default settings, modified for the simulation of the EMTiming system (see App. B in Ref. [37]). We simulate the full GMSB model with the setting MSEL=39 with the masses calculated with ISASUGRA [38]. We use the detector calibrations of p1 to p13 for all MC samples with tune-A and Min-Bias to properly simulate effects due to vertex swap and $\not\!\!E_T$ cleanup cut. Studies, see Appendix C, indicate that there is no acceptance dependence on the luminosity, thus we ignore the addition of systematics due to not including through p17. Each sample contains 133,330 events which yields a statistical uncertainty of $\sim$1% since the probability for signal events to pass our final kinematic cuts is $\sim$8%. For our analysis we only consider $\tilde{\chi}_1^0$'s lifetimes up to 2 ns since *cdfSim* does not simulate χ^2_{CES} correctly for a high incident angle photons from higher lifetime $\tilde{\chi}_1^0$'s [37]. Also the next generation delayed photon analysis will deal with high lifetimes.

The total event accepance, $A_{Signal\ MC}$, is used when calculating the cross section limits, and is quantitatively defined by:

$$A_{Signal\ MC}(\%) = \frac{N_{\mathrm{events}}^{\mathrm{passing\ all\ cuts}}}{N_{\mathrm{events}}^{\mathrm{total\ produced}}}. \tag{20}$$

The breakdown of events passing each of the selection cuts for an example GMSB point at $m(\tilde{\chi}_1^0) = 140$ GeV and $\tau(\tilde{\chi}_1^0) = 0$ ns is shown in Table 15. For completeness we have included the results for the final event selection, determined in Section 6.

Figure 13 shows the $\not\!\!E_T$, MetSig, H_T and $\Delta\phi(\gamma_1, \gamma_2)$ distributions for GMSB signal MC after the preselection cuts.

Requirement	Events passed	$A_{\text{Signal MC}}$ (%) ($m_{\tilde{\chi}_1^0} = 140$ GeV and $\tau_{\tilde{\chi}_1^0} = 0$ ns)
Sample events	133330	100.0
Two EM Objects and $\lvert z_{vertex}\rvert < 60\ cm$	124771	93.6
Photon fiducial and Standard ID cuts	18270	13.7
Phoenix Rejection and PMT cuts	17625	13.2
Beam Halo and Cosmic Rejection cuts	17612	13.2
Vertex Swap and $\not\!\!E_T$ Cleanup cuts	17049	12.8
MetSig>3	12610	9.5
H_T>200 GeV	11913	8.9
$\Delta\phi(\gamma_1, \gamma_2)<\pi - 0.35$	10395	7.8

Table 15: Summary of the event reduction for a GMSB example point in the $\gamma\gamma+\not\!\!E_T$ final state. We have included the final, optimized cuts for completeness.

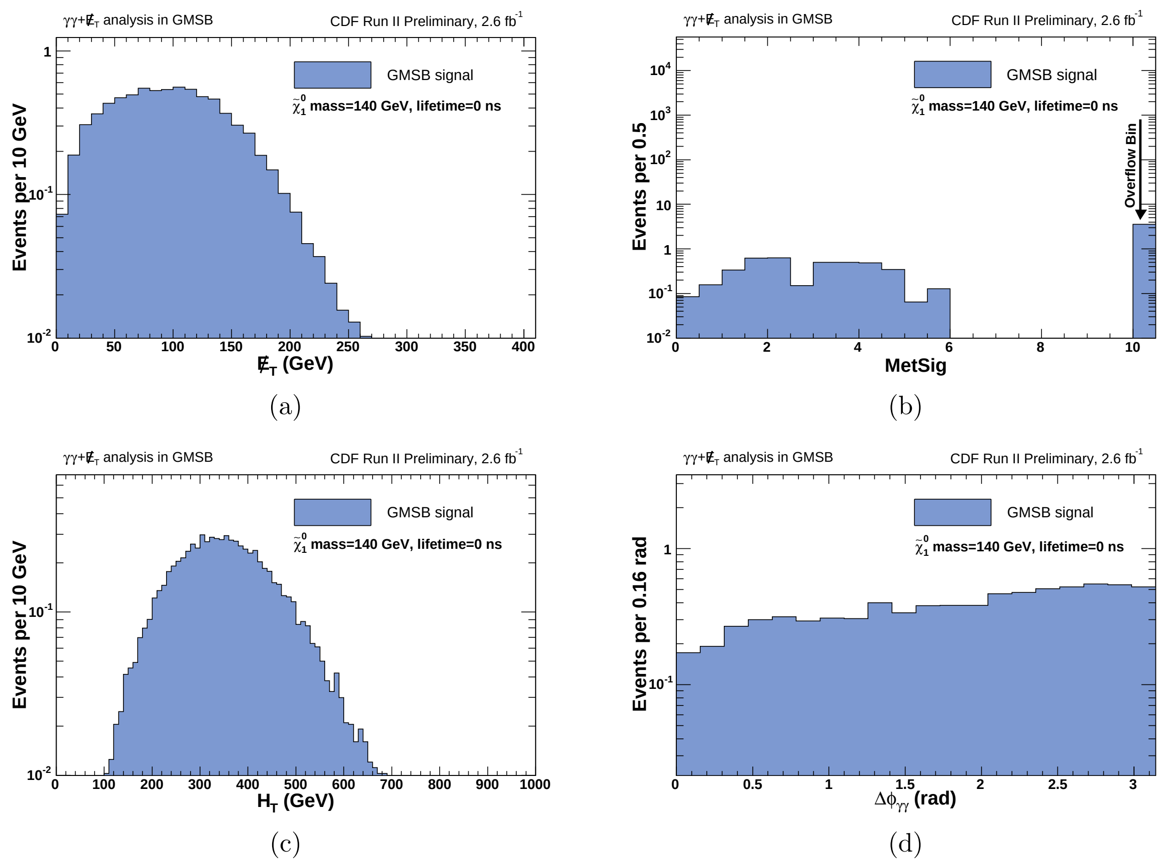

(a) (b) (c) (d)

Figure 13: The $\not\!\!E_T$, MetSig, H_T and $\Delta\phi(\gamma_1, \gamma_2)$ distributions for GMSB signal MC after the preselection requirements, but normalized by the NLO cross section and luminosity. In Figure (b) there are a subset of events with low MetSig (< 7) due to the fact that while the non-interacting particles are highly energetic, they might not have small η, or there are two (or more) that point in opposite directions and cancel each other out, giving small $\not\!\!E_T$. The second region, above about 7, including the overflow bins at 10, is due to events with large $\not\!\!E_T$.

5 Estimation of the Systematic Uncertainties

Since we define the sensitivity of the search to be equal to the expected 95% C.L. cross section limits, we need the uncertainties for the trigger, luminosity, background and acceptance. As mentioned in Section 2 (more detail in Appendix C), with our combination of triggers and high E_T photons we take a trigger efficiency of 100% with negligible error [28]. The systematic uncertainty on the luminosity is taken to be 6% with major contributions from the uncertainties on the CLC acceptance from the precision of the detector simulation and the event generator [39]. The systematic uncertainty on the background in the signal region is determined from our understanding of both the collision and non-collision sources, as described in Section 3. The background uncertainty is evaluated for every set of cuts in the optimization procedure. The acceptance and cross section uncertainties are estimated in the subsections below. The results are summarized in Table 16 for an example GMSB point of $m(\tilde{\chi}_1^0) = 140$ GeV and $\tau(\tilde{\chi}_1^0) = 0$ ns. All uncertainties are consistent with the GMSB diphoton analysis in Ref. [17] unless otherwise noted. We take the systematic uncertainty to be constant for all masses.

Factor	Relative Systematic Uncertainty (%)
Acceptance:	
Diphoton ID and Isolation	5.4
ISR/FSR	3.9
JES	1.6
MetSig parameterizations	0.7
PDFs	0.4
Total	6.9
Cross section:	
PDF	7.6
Renormalization scale (Q^2)	2.6
Total	8.0

Table 16: Summary of the systematic uncertainties on the acceptance and production cross section for an example GMSB point at $m(\tilde{\chi}_1^0) = 140$ GeV and $\tau(\tilde{\chi}_1^0) = 0$ ns. In the limit calculators we get the full limit from taking into account the systematic uncertainties on both the production cross section and the acceptance in quadrature to get a 10.6% uncertainty on the "acceptance" [46].

5.1 Acceptance Uncertainties

There are a number of effects that can cause our estimate of the acceptance to be systematically mis-estimated. We identify them here, in order of decreasing magnitude, and explain how they are estimated. The dominant uncertainty on the acceptance is the photon ID and isolation.

5.1.1 Photon ID and Isolation Efficiencies

The photon ID and isolation variables are imperfectly modeled in *cdfSim*. This has been studied in detail elsewhere. We take a systematic uncertainty of 1.8% for the photon ID and 2.0% for the isolation efficiencies, as described in Ref. [40, 41], in quadrature for a total of 2.7% uncertainty per photon. Since there are two photons we take the total systematic uncertainty to be $2 \times 2.7\% = 5.4\%$. This represents an improvement over the 202 pb^{-1} result [17] due to improved understanding of the detector.

5.1.2 ISR/FSR (Initial and Final State Radiation)

Initial state radiation (ISR) caused by a gluon radiating from an incoming parton or final state radiation (FSR) from an outgoing jet can both make the E_T spectrum of the final state particles softer than expected without radiation. This can cause the photon, the jets or the $\not\!\!E_T$ to be systematically more or less likely to pass the kinematic requirements. The effect carries a non-negligible theoretical uncertainty and is estimated using the standard CDF procedure by varying the Sudakov parameters as described in [42]. Doing so we find a variation in the acceptance, taken to be the systematic uncertainty, of 3.9%.

5.1.3 JES (Jet Energy Scale)

Since we allow jets with a corrected $E_T > 15$ GeV to be counted in our H_T and MetSig calculations we have studied the change in acceptance if the jet energy is mismeasured. The following effects are taken into account: relative jet energy, underlying event, multiple interaction, absolute energy scale, out-of-cone and splash-out. The standard procedure at CDF [34] varies each correction factor independently by $\pm 1\sigma$. The resulting variation on the acceptance is $\pm 1.6\%$.

5.1.4 MetSig parameterization and calibration

The MetSig calibrations and unclustered-energy parameterizations are slightly different for data and MC (See Figs. 10 and 16 in Ref. [21]). To estimate the magnitude of this uncertainty on the acceptance we compare the acceptance using the most different sets and find the uncertainty on the acceptance to be 0.7%.

5.1.5 PDFs (Structure Functions)

In an event where proton and antiproton bunches collide it is mostly a single subparticle of the (anti-)proton, a parton (quark or gluon), that participates in the hard collision and produces a high center-of-mass energy event. The momentum fraction, described by parton distribution function (PDFs), that is carried by each of the partons in the proton or antiproton is not perfectly understood. If affects both the rate at which a process happens (the production cross section) and the kinematics of the outgoing final state particles (the acceptance of the event selection criteria).

To estimate the magnitude of this effect on the acceptance we use the standard technique of evaluating the uncertainty, event-by-event, the momentum fraction of the colliding parton using a standardized "PDF-set" by the `CTEQ` collaboration (`CTEQ-5L`) [43]. As only the newer PDF-set version `CTEQ-6M` contains 90% confidence intervals for each eigenvector, the total uncertainty is estimated using a standard procedure by reweighting the parton momenta of the original `CTEQ-5L` set and varying the PDFs using the uncertainties from `CTEQ-6M` as described in Ref. [43]. For the example GMSB point we get a relative uncertainty of $+0.3\%$ -0.4% [44] on the acceptance. We take the larger value to estimate the uncertainty conservatively.

5.2 Production Cross Section Uncertainties

The production cross section uncertainty is dominated by the uncertainty on the PDFs.

5.2.1 PDFs (Structure Functions)

Using the same methods in subsection 5.1.5, but considering the total production cross section calculation for the example GMSB point, we get a relative uncertainty of $+7.6\%$ -7.3% on the cross section. We take the larger value to estimate the uncertainty conservatively. This uncertianty is a little bit bigger than what we had in the delayed photon analysis ($\sim$5.9% for $m_{\tilde{\chi}_1^0} = 100$ GeV) since our example point uses a heavier mass.

5.2.2 Q^2 (Renormalization Scale)

While the dominant GMSB production mechanisms are via electroweak processes (see Figure 1), the probability that QCD processes occur via gluon emission and higher-order loops depend sensitively on the energy scale at which the process happens. In PYTHIA [11] events are generated using a fixed renormalized (q^2) scale of $\hat{s}$. However, the NLO cross section, which is calculated with PROSPINO2 [45], varies as a function of the renormalization scale. The variation of the NLO production cross section observed by changing the scale from $0.25{\cdot}q^2$ to $4{\cdot}q^2$ is calculated to be 2.6% for the example GMSB point.

5.3 Summary of the Systematic Uncertainties

All systematic erros are combined in quadrature to give 6.9% on the acceptance and 8.0% on the production cross section. These are combined in quadrature to give a total systematic uncertainty of 10.6% used in the limit calculatiors for the "acceptance". The individual results are given in Table 16.

6 Optimization and Expected Limits

Now that the background estimation methods are determined and the signal acceptance is available for a given set of cuts, along with their uncertainties, an optimization procedure can be readily employed. Using only general cuts we can conduct a robust and partially model independant search. We can then optimize that set of cuts before unblinding the signal region,

We choose to optimize for MetSig, H_T, and $\Delta\phi(\gamma_1, \gamma_2)$ cuts for following reasons[5]:

- MetSig:
  As described in Section 3, this cut gets rid of most of the QCD background with fake $\not\!\!E_T$.

- H_T:
  In GMSB production heavy gaugino pair-production dominates, and the gauginos decay to light, but high E_T, final state particles via cascade decays. Thus, GMSB signal has lots of H_T compared to SM backgrounds, which are dominated by QCD and electroweak backgrounds which do not have lots of high E_T objects.

- $\Delta\phi(\gamma_1, \gamma_2)$:
  Electroweak backgrounds with large H_T are typically a high E_T photon recoiling against $W \to e\nu \to \gamma_{fake} + \not\!\!E_T$, which means the gauge boson decay is highly boosted. Thus, the two photon candidates in the final state are mostly back-to-back. Also, pairs of high E_T photons with large H_T from QCD background are mostly back-to-back with fake $\not\!\!E_T$ or from the wrong vertex. The $\Delta\phi(\gamma_1, \gamma_2)$ cut reduces both these backgrounds.

We optimize for all kinematic requirements simultaneously at each GMSB parameter point. Once we have the optimal values at each point we then check that a single choice is robust enough to be applied throughout the parameter space for simplicity. By estimating our sensitivity using the 95% C.L. expected cross section limits on GMSB models, in the no-signal assumption, we find an optimal set of cuts before unblinding the signal region. We use the standard CDF cross section limit calculator [46] to calculate the limits, taking into account the predicted number of background events, the acceptance, the luminosity and their systematic uncertainties (see Section 5). We take

$$\sigma_{95}^{\mathrm{exp}} = \textstyle\sum_{N_{obs}=0}^{\infty} \sigma_{95}^{obs}(\mathrm{cut}) \times \mathrm{Prob}(N_{obs}, N_{exp} = \mu) \tag{21}$$

$$\mathrm{RMS}^2 = \textstyle\sum_{N_{obs}=0}^{\infty} (\sigma_{95}^{obs}(\mathrm{cut}) - \sigma_{95}^{\mathrm{exp}})^2 \times \mathrm{Prob}(N_{obs}, N_{exp} = \mu) \tag{22}$$

where N_{obs} is the number of observed events in the pseudoexperiment, μ is the mean of the number of expected events as a function of the cuts and σ_{95}^{obs} denotes the cross section limit if N_{obs} were observed. Each are a function of the cut choices, so the expected cross section limit is also just a function of the cuts ($0 \le$ MetSig ≤ 10 in steps of 1, $0 \le H_T \le 400$ GeV in steps of 25 GeV, and $2.4 \le \Delta\phi(\gamma_1, \gamma_2) \le 3.14$ rad in steps of 0.05 rad).

[5] Many other cuts were considered, including $\not\!\!E_T$, $\Delta\phi(\gamma 1, \not\!\!E_T)$, $\Delta\phi(\gamma 2, \not\!\!E_T)$, $\Delta\phi(jet, \not\!\!E_T)$, $E_T^{\gamma 1}$, $E_T^{\gamma 2}$ and N_{jets} (number of jets), but these yield negligible gain and add additional systematic uncertainties.

For each GMSB point the minimum expected cross section limit defines our set of optimal cuts for that mass and lifetime combination. The exclusion region is defined by the region where the production cross section is above the 95% C.L. cross section limit. The mass/lifetime limit is where the two cross. We chose MetSig >3, $H_T>200$ GeV, $\Delta\phi(\gamma_1, \gamma_2)<\pi - 0.35$ rad as this maximizes the mass limit for $\tau = 0$. As an illustration that the optimization minimizes the expected cross section limit in all three variables, Figures 15-(a), (c), and (e) show the expected limit as a function of a cut while keeping all other cuts fixed at the optimized values around the mass limit. Indicated in green is the 8.0% uncertainty-band on the production cross section. In yellow we show the expected statistical variation in the cross section limit using the data in Table 17 and the RMS definition in Eq. 22. We decided to use a single set of cuts before we open the box based on the expectation that they will yield the largest expected exclusion region without significant loss of sensitivity to lower mass or higher lifetime scenarios.

With these cuts we predict 1.38±0.44 background events with 0.92±0.37 from electroweak sources with real $\not\!\!E_T$, 0.46±0.24 from QCD with fake $\not\!\!E_T$ and $0.001^{+0.008}_{-0.001}$ from non-collision sources. Table 18 shows the raw numbers and calculations for the individual electroweak background sources after the optimal cuts. They are summarized in Table 19. Note that we calculate the electroweak global scale factor for each different set of cuts and its distribution is shown in Figure 14. The dominant electroweak contribution is $Z\gamma \to \nu\nu\gamma$ which produces a total of 0.26±0.08 events. The QCD background contributions are given in Tables 20 and are dominated by energy measurement fluctuations in the $\not\!\!E_T$, estimated using the *Met Model* to have a rate of 0.40±0.20 events. The non-collision background calculations are shown in Table 21 and are dominated by cosmics which have a rate of 0.001±0.001. Table 22 provides the final summary.

Table 23 shows the expcted cross section limits, acceptance and production cross section of each GMSB point simulated, along with the predicted backgrounds. Figures 15-(b), (d), and (f) show the distributions of each optimization variable normalized to the number of expected events, after applying all optimized cuts. We compare the background distribution before unblinding the signal region and the expected signal in the signal region for an example GMSB point at $m(\tilde{\chi}_1^0) = 140$ GeV and $\tau(\tilde{\chi}_1^0) = 0$ ns. Taking into account the errors we expect an acceptance of (7.80±0.54)%. In the next section, we unblind the signal region and set limits on GMSB models.

We note that we do not do a separate optimization for non-zero lifetimes. Rather we simply estimate the sensitivity of our analysis to these scenarios for lifetimes up to 2 ns. The expected results are given in Table 23.

N_{obs}	Probability	$\sigma_{obs}(N)$ (fb)
0	0.252	15.1
1	0.347	20.7
2	0.240	26.8
3	0.110	33.4
4	0.038	40.3
5	0.002	48.2

Table 17: The 95% C.L. cross section limit as a function of the hypothetically observed number of events, after optimization. The Poisson probability for this number of events is based on the background expectation of 1.38 events. The acceptance and cross section limit are calculated for an example GMSB point of m($\tilde{\chi}_1^0$)=140 GeV/c^2 and $\tau(\tilde{\chi}_1^0)$=0 ns. The expected limit and its variation are calculated as shown in [46] with Eqs. 21 and 22. With these numbers we get an expected cross section limit of 22.1 fb and an RMS on the limit of 7.6 fb.

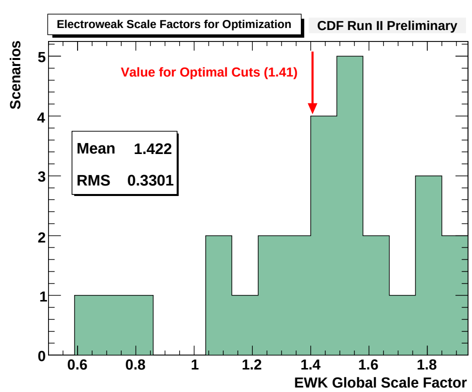

Figure 14: The electroweak global scale factor distributions for each different set of cuts considered in our optimization procedure. Note that our optimal point is near the mean of the distribution, consistent with no bias in the optimization. The RMS is consitent with uncertainties on the expectation from the E/p variation.

Background Source (Charged Leptons)	SF_i	EWK $\gamma\gamma + \not\!\!E_T$ signal		$0.8 < E/p < 1.2$ for $e\gamma$		$0.0 < E/p < 2.0$ for $e\gamma$	
		MC Events	$\mathrm{N}^{\mathrm{EWK-MC}}_{\mathrm{signal},i} \cdot \mathrm{SF}_i$	MC Events	$\mathrm{N}^{\mathrm{MC}}_{e\gamma,\mathrm{signal},i} \cdot \mathrm{SF}_i$	MC Events	$\mathrm{N}^{\mathrm{MC}}_{e\gamma,\mathrm{signal},i} \cdot \mathrm{SF}_i$
$W(e\nu)+\gamma$	0.064	1	0.064±0.064	83	5.270±0.578	99	6.286±0.632
$W(\mu\nu)+\gamma$	0.060	0	0.00±0.060	0	0.00±0.060	0	0.00±0.060
$W(\tau\nu)+\gamma$	0.061	1	0.061±0.061	3	0.183±0.105	3	0.183±0.105
$Z(ee)+\gamma$	0.004	3	0.012±0.007	64	0.252±0.031	76	0.299±0.034
$Z(\mu\mu)+\gamma$	0.004	35	0.138±0.023	5	0.020±0.009	8	0.032±0.011
$Z(\tau\tau)+\gamma$	0.004	25	0.099±0.020	93	0.368±0.038	129	0.511±0.045
$Z(\nu\bar{\nu})+\gamma$	0.0010	183	0.183±0.013	0	0.00±0.001	0	0.00±0.001
$W(e\nu)$ no ISR/FSR	0.210	0	0.00±0.035	4	0.84±0.42	5	1.05±0.47
$W(\mu\nu)$ no ISR/FSR	0.308 (0.699)	0	0.00±0.051	0	0.00±0.699	0	0.00±0.699
$W(\tau\nu)$ no ISR/FSR	0.296	0	0.00±0.049	0	0.00±0.296	0	0.00±0.296
$Z(ee)$ no ISR/FSR	0.056	0	0.00±0.056	1	0.056±0.056	1	0.056±0.056
$Z(\mu\mu)$ no ISR/FSR	0.088 (0.126)	0	0.00±0.088	0	0.00±0.126	0	0.00±0.126
$Z(\tau\tau)$ no ISR/FSR	0.039	1	0.039±0.039	1	0.039±0.039	1	0.039±0.039
$t\bar{t}$ (incl.)	0.0023	25	0.058±0.012	621	1.453±0.058	739	1.729±0.064
$\sum_{i=0}^{n} \mathrm{N}^{\mathrm{EWK-MC}}_{\mathrm{signal},i} \cdot \mathrm{SF}_i$			0.65±0.15				
$\mathrm{N}^{\mathrm{MC}}_{e\gamma,\mathrm{signal}} = \sum_{i=0}^{n} \mathrm{N}^{\mathrm{MC}}_{e\gamma,\mathrm{signal},i} \cdot \mathrm{SF}_i$					8.49±1.06		10.18±1.11
$\mathrm{N}^{\mathrm{Data}}_{e\gamma,\mathrm{signal}}$				12		16	
$\frac{\mathrm{N}^{\mathrm{Data}}_{e\gamma,\mathrm{signal}}}{\mathrm{N}^{\mathrm{MC}}_{e\gamma,\mathrm{signal}}}$				1.41±0.44		1.57±0.43	
The Final EWK Prediction $\mathrm{N}^{\mathrm{EWK}}_{\mathrm{signal}} = \sum_{i=0}^{n} \mathrm{N}^{\mathrm{EWK-MC}}_{\mathrm{signal},i} \cdot \mathrm{SF}_i \cdot \left(\frac{\mathrm{N}^{\mathrm{Data}}_{e\gamma,\mathrm{signal}}}{\mathrm{N}^{\mathrm{MC}}_{e\gamma,\mathrm{signal}}}\right)$	=(0.65±0.15)×(1.41±0.47) 0.92±0.21±0.30 (Expected Rate±Stat±Sys)						

Table 18: The charged electroweak background calculations for the optimal cuts ($H_T > 200$ GeV, MetSig > 3.0 and $\Delta\phi(\gamma_1, \gamma_2) < \pi - 0.35$). The SF_i scale factors are taken from Table 11. All errors are stat. only unless noted otherwise. The final electroweak global scale factor with E/p variations is estimated for each different set of optimal cuts. Figure 14 shows the variation of the electroweak global scale factor for a number of different optimization cuts. We take a systematic uncertainty on the global electroweak scale factor of 0.47 ($=\sqrt{0.44^2 + (1.57 - 1.41)^2}$). These results are summarized in Table 19.

Background Source	Expected Rate±Stat±Sys
$W(l\nu)+\gamma$	0.176±0.149±0.059
$Z(ll)+\gamma$	0.351±0.044±0.117
$Z(\nu\nu)+\gamma$	0.26±0.03±0.08
$W(l\nu)$ no ISR/FSR	0.0±0.111±0.001
$Z(l\nu)$ no ISR/FSR	0.055±0.096±0.018
$t\bar{t}$	0.082±0.017±0.027
EWK combined	0.92±0.21±0.30

Table 19: Summary of the scaled electroweak background estimations after optimization, taken from Table 18.

Background Source	Scale Factor	MC Events	*Met Model* Pred.	Normalized Pred.
	$\mathrm{SF_{QCD}}$	$\mathrm{N_{signal}^{PATH-MC}}$	$\mathrm{N_{signal}^{MM-MC}}$	$\mathrm{N_{signal}^{PATH}}$
Pathology	0.134±0.007	1	0.527	0.063±0.092±0.003
QCD from *Met Model*				0.40±0.20±0.10
Total QCD				0.46±0.22±0.10

Table 20: Summary of the QCD background estimations after optimization. The normalized prediction from pathologies is given by $\mathrm{N_{signal}^{PATH}} = (\mathrm{N_{signal}^{PATH-MC}} - \mathrm{N_{signal}^{MM-MC}}) \cdot \mathrm{SF_{QCD}}$. To avoid double counting the number of events from energy mis-measurements predictied by the *Met Model* we take $\mathrm{N_{signal}^{MM-MC}} = \mathrm{N_{signal}^{noMetSig\ cut}} \cdot \mathrm{R_{MetSig=3}^{exp}} = 527 \times 0.001$, where $\mathrm{R_{MetSig=3}^{exp}} = 0.1\%$, using Eq.(3), described in Section 3.2.1. The *Met Model* prediction is given by $\mathrm{N_{signal}^{MetModel}} = \frac{\mathrm{N_{signal}^{pseudo}}}{\mathrm{N_{pseudo}}} = \frac{4}{10} = 0.40 \pm 0.20$ (stat. only).

Background Source	Total Rejection Fracton	Events Passed	Normalized Pred.
i	SF_i	$\mathrm{N_{kinematic}^{\mathit{i}-control}}$	$\mathrm{N_{signal}^{\mathit{i}}}$
Beam Halo	0.008±0.008	0	0.0+0.008±0.001
Cosmic Rays	0.001±0.001	1	0.001±0.001±0.001
Non-Collision			$0.001^{+0.008}_{-0.001} \pm 0.001$

Table 21: Summary of the non-collision background estimations after optimization. The normalized prediction of the beam halo (cosmic ray) is given by $\mathrm{N_{signal}^{\mathit{i}}} = \mathrm{N_{kinematic}^{\mathit{i}-control}} \cdot \mathrm{SF}_i$, where i=BH or CR, described in Section 3.4.

Background Source	Expected Rate±Stat±Sys
Electroweak	0.92±0.21±0.30
QCD	0.46±0.22±0.10
Non-Collision	$0.001^{+0.008}_{-0.001} \pm 0.001$
Total	1.38±0.30±0.32

Table 22: Summary of the combined background estimations after optimization. Note we have ignored the small asymetric uncertainty in the total calculation.

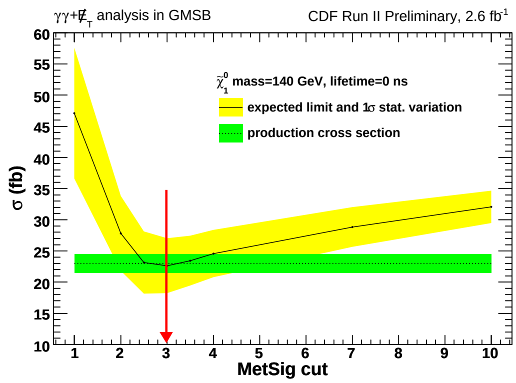

(a)

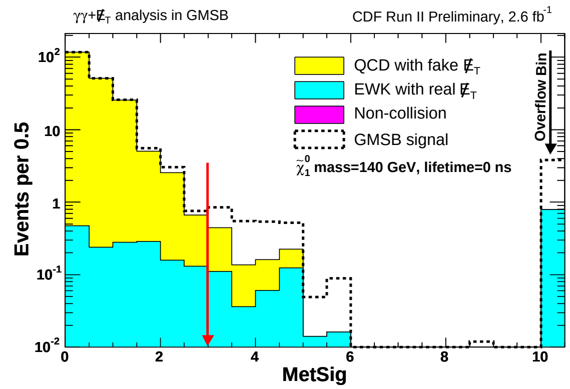

(b)

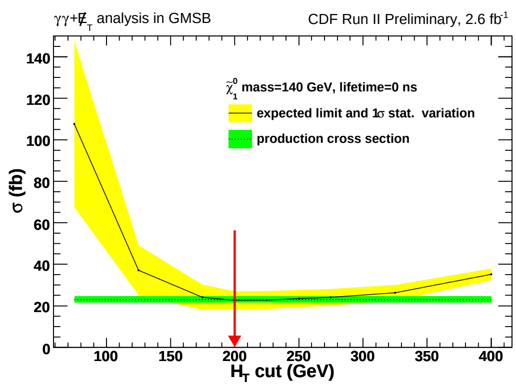

(c)

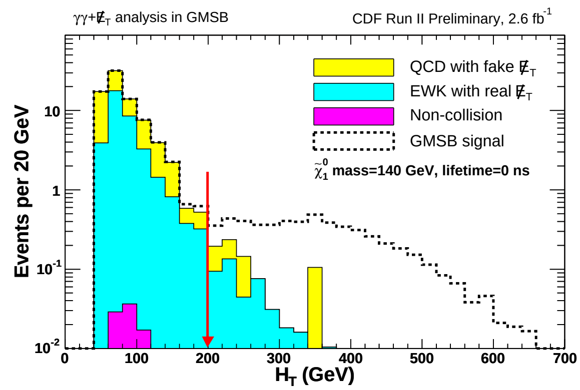

(d)

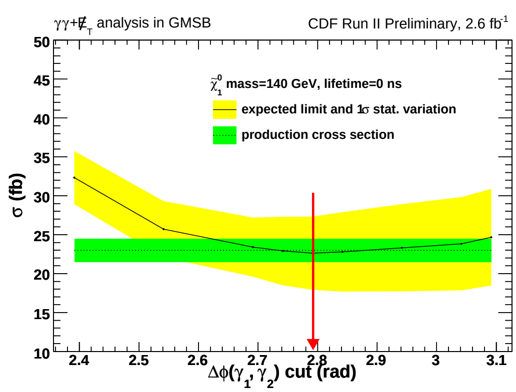

(e)

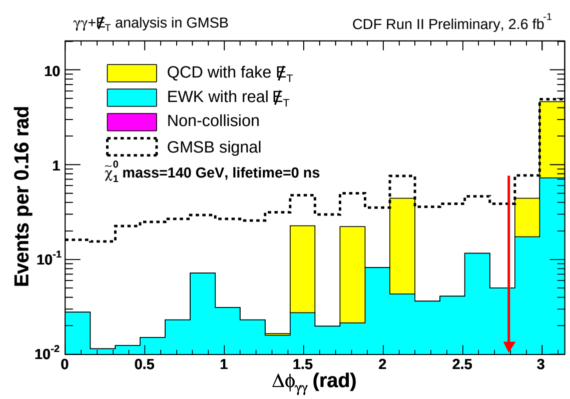

(f)

Figure 15: The expected 95% C.L. cross section limit as a function of the MetSig (a), H_T (c), and $\Delta\phi(\gamma_1, \gamma_2)$ (e) requirements for a GMSB example point ($m(\tilde{\chi}_1^0) = 140$ GeV and $\tau(\tilde{\chi}_1^0) = 0$ ns). All other cuts held at their optimized values. The optimal cut is where the expected cross section is minimized. Indicated in green is the 8.0% uncertainty-band for the production cross section (see Table 16) and in yellow is the RMS (See Eqn. 22). The N-1 predicted kinematic distributions after the optimized requirements are shown in Figure (b), (d), and (f).

$m_{\tilde{\chi}}$ (GeV/c^2)	$\tau_{\tilde{\chi}}$ (ns)	Acceptance (%)	Background	$\sigma_{95}^{\mathrm{exp}}$ (fb)	$\sigma_{95}^{\mathrm{obs}}$ (fb)	$\sigma_{95}^{\mathrm{prod}}$ (fb)
70	0	2.04±0.43		81.92	57.20	
70	1	1.85±0.18		90.92	62.99	999.9
70	2	1.41±0.14		124.5	86.30	
80	0	4.29±0.43		40.83	28.22	
80	1	3.71±0.37		45.59	31.51	524.6
80	2	2.82±0.28		60.02	41.48	
90	0	5.12±0.51		32.76	22.65	
90	1	4.42±0.44	Total: 1.38±0.44	38.32	26.48	286.8
90	2	3.48±0.34	(0 observed)	48.60	33.59	
100	0	6.74±0.67		25.12	17.36	
100	1	6.40±0.64	EWK: 0.92±0.37	26.46	18.29	169.0
100	2	4.93±0.49	QCD: 0.46±0.24	34.25	23.67	
110	0	7.08±0.71	Non-Collision:	23.88	16.53	99.47
110	1	7.06±0.71	$0.001^{+0.008}_{-0.001}$	23.95	16.54	
120	0	7.21±0.72		23.97	26.24	
120	2	5.64±0.56		29.97	20.71	58.38
130	0	7.86±0.79		21.90	14.84	
130	1	8.05±0.80		21.40	14.49	36.23
130	2	5.95±0.60		28.44	19.67	
140	0	7.80±0.78		22.62	15.11	
140	1	7.87±0.79		21.94	14.87	22.97
140	2	6.08±0.61		27.86	19.26	
150	0	7.95±0.79		21.25	14.67	14.54

Table 23: The acceptance and expected cross section limits for various simulated GMSB points for the final selection requirements. For completeness we have included both the expected and observed number of events and cross section limits from Section 6. Note we use the same analysis for all masses and lifetimes up to 2 ns.

7 Data, Cross Section Limits and Final Results

In this section we unblind the signal region, set cross section limits and show the exclusion regions as a function of $m_{\tilde{\chi}_1^0}$ and $\tau_{\tilde{\chi}_1^0}$ for GMSB models.

7.1 The Data and Cross Section Limits

After all optimal cuts we open the box and observe no events in the signal region, consistent with the expectation of 1.38±0.44 events. Figure 16 shows the kinematic distributions for the background and signal expectations along with the data. The data appears to be well modeled by the background precdiction alone.

7.2 The GMSB Exclusion Region

Figure 17 shows the predicted and observed cross section limits along with the NLO production cross sections (see Table 16) as a function of the $\tilde{\chi}_1^0$ mass at a lifetime of 0 ns and as a function of the $\tilde{\chi}_1^0$ lifetime at a mass of 140 GeV/c^2. Indicated in green is the 8.0% uncertainty-band on the production cross section. In yellow we show the expected variation in the expected cross section limit using the data in Table 17 and the RMS definition in Eq. 22. Since the number of observed events is below expectations the observed limits are slightly better than the expected limits. The $\tilde{\chi}_1^0$ mass reach, based on the predicted (observed) number of events is 141 GeV/c^2 (149 GeV/c^2), at a lifetime of 0 and 1 ns. We do not consider lifetimes above 2 ns for the reasons mentioned in Section 4 as well as the expectation that most of the parameter space in high lifetimes there should be excluded by searches in single delayed photon analysis [7, 19]. Fig. 18 shows the 95% C.L. NLO exclusion region as a function of mass and lifetime of $\tilde{\chi}_1^0$ using the fixed choice of cuts from the optimization for both for the predicted and observed number of background events. These limits extend the reach beyond the delayed photon results [19] and well beyond those of DØ searches at $\tau = 0$ [18] and the limit from ALEPH/LEP [16], and are currently the world's best.

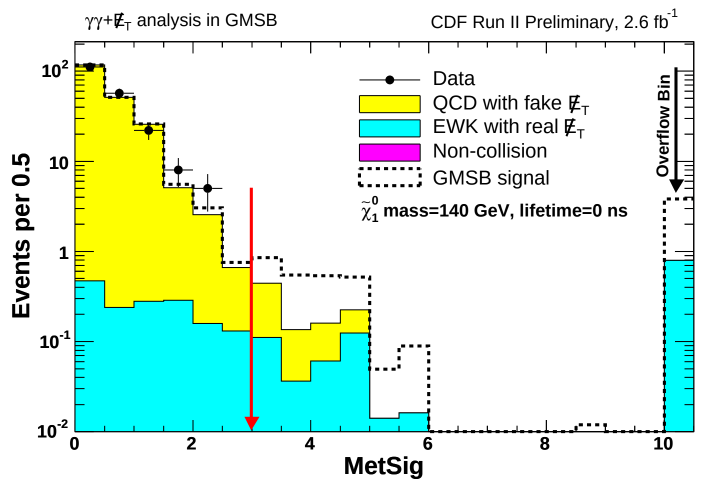

(a)

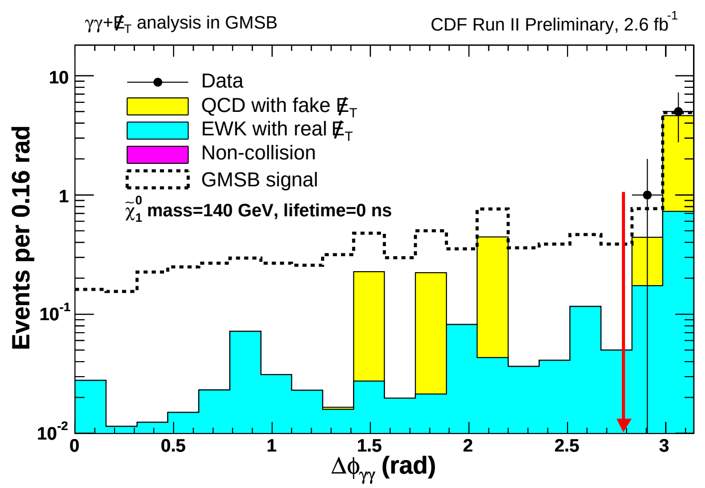

(b)

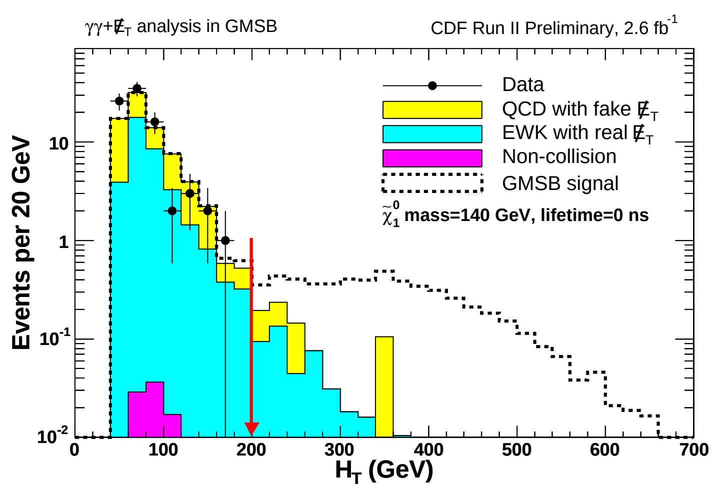

(c)

Figure 16: The same N-1 plots as Figure 15, but including the data. Each variable is plotted through the whole region while holding other variables at the optimal cuts. There is no evidence for new physics and the data is well modeled by backgrounds alone.

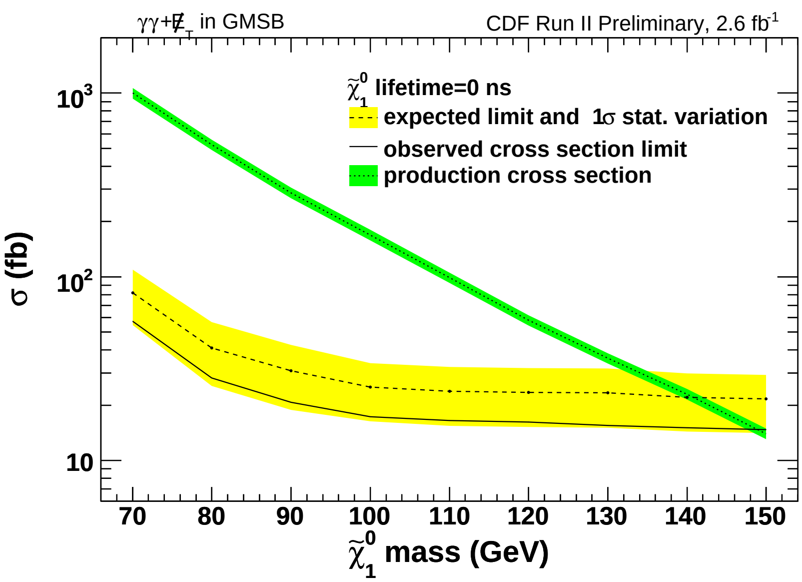

(a)

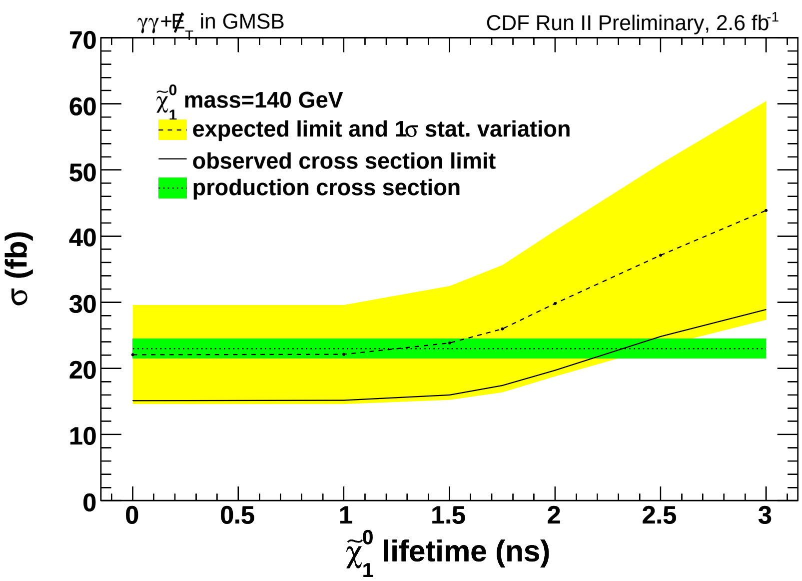

(b)

Figure 17: The predicted and observed cross section limits as a function of the $\tilde{\chi}_1^0$ mass at a lifetime of 0 ns (a) and as a function of the $\tilde{\chi}_1^0$ lifetime at a mass of 140 GeV/c^2 (b). Indicated in green is the 8.0% uncertainty-band for the production cross section (see Table 16), in yellow the RMS variation in the expected on the cross section limit.

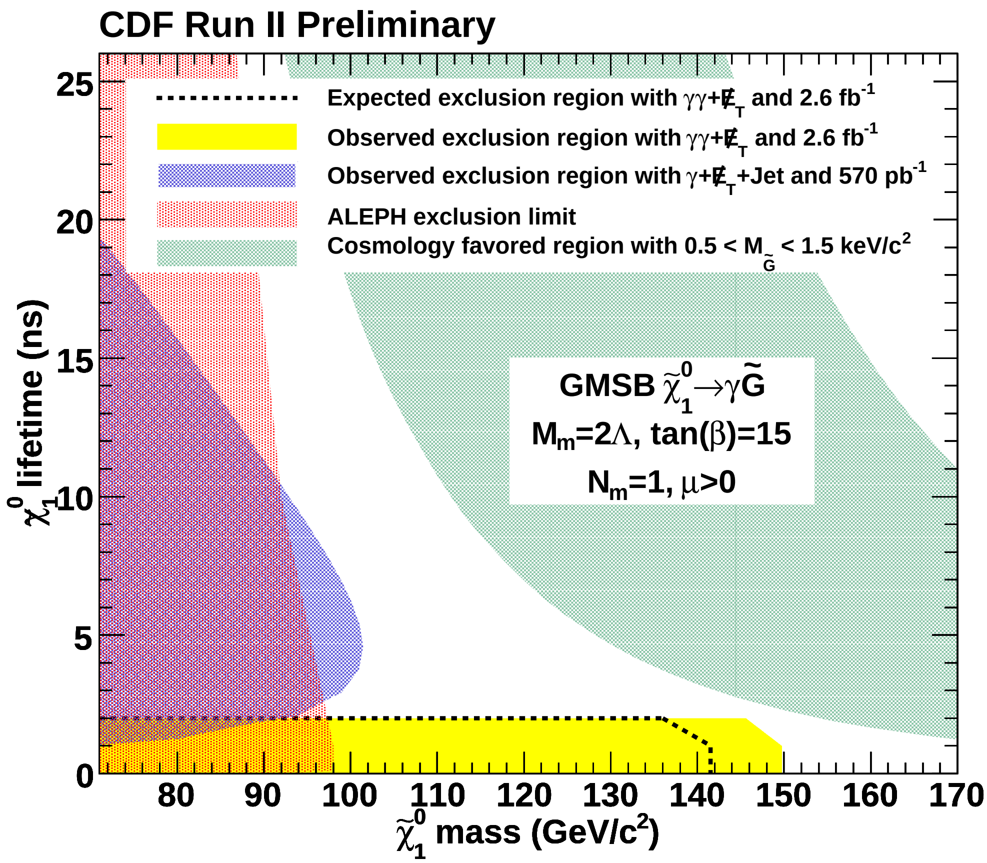

Figure 18: The predicted and observed exclusion region along with the limit from ALEPH/LEP [16] and the $\gamma + \not\!\!E_T + jet$ delayed photon analysis [19]. We have a mass reach of 141 GeV/c^2 (predicted) and 149 GeV/c^2 (observed) at the lifetime up to 1 ns. The green shaded band shows the parameter space where $0.5 < m_{\tilde{G}} < 1.5$ keV/c^2, favored in cosmologically consistent models [4].

8 Conclusions and Prospects for the Future

We have set limits on low $\tilde{\chi}_1^0$ lifetime GMSB models using a search for anomalous events in the $\gamma\gamma+\not\!\!E_T$ final state. Candidate events were selected based on the new $\not\!\!E_T$ resolution model technique, the EMTiming system and a full optimization procedure. We found 0 event using 2.59 fb^{-1} of data in run II which is consistent with the background estimate of 1.38$\pm$0.44 events from the Standard Model expectations. We showed exclusion regions in the $\tau_{\tilde{\chi}_1^0}$ vs. $m_{\tilde{\chi}_1^0}$ plane and set limits on GMSB models with a $\tilde{\chi}_1^0$ mass reach of 149 GeV/c^2 at a $\tilde{\chi}_1^0$ lifetime of 0 ns. Our results extend the world sensitivity to these models.

To investigate the prospects of a search at higher luminosity we calculate the expected cross section limits assuming all backgrounds scale linearly with luminosity while their uncertainty fractions remain constant. Figure 19 shows the predicted exclusion region for a luminosity of 10 fb^{-1}. For higher lifetimes (above $\sim$2 ns) the next generation delayed photon analysis will extend the sensitiviy taken from Ref. [19] and then will combine these results for completeness.

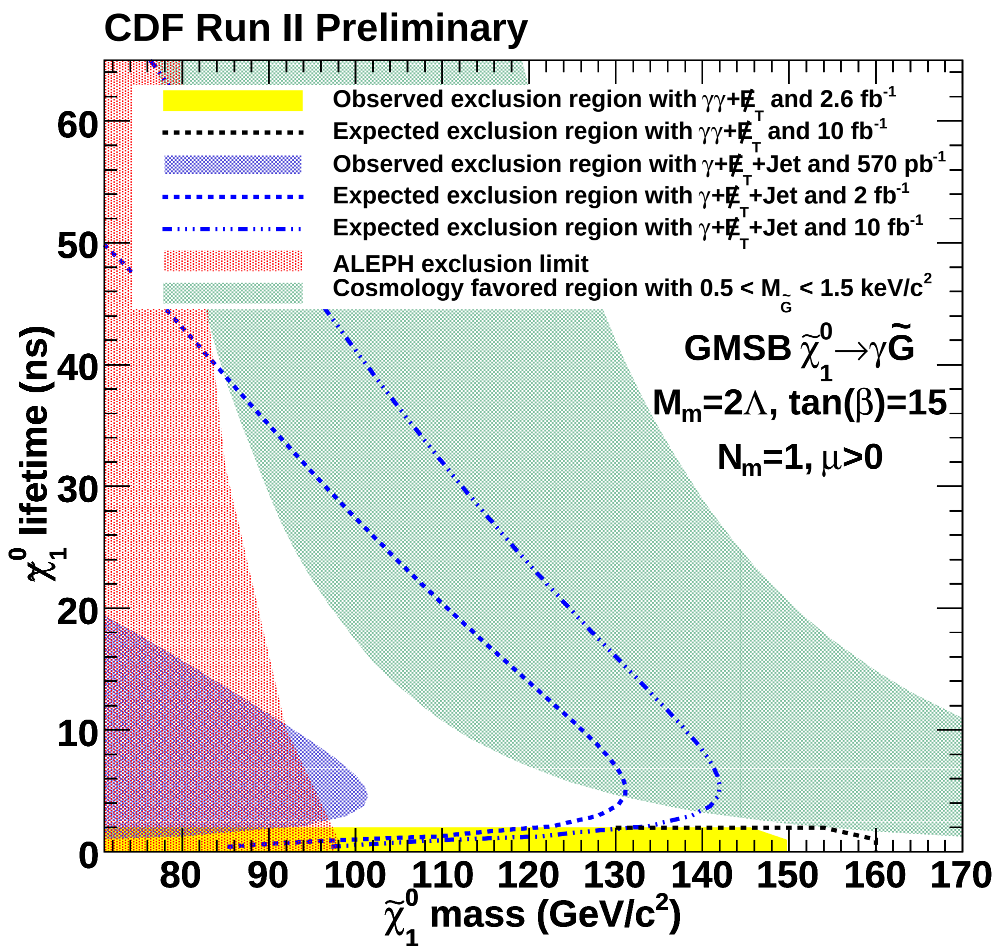

Figure 19: The black dashed line shows the prediction of the exclusion region limit after a scaling of the background prediction and the uncertainties for a luminosity of 10 fb^{-1}. The blue dashed lines show the prediction of the exclusion region limits from the delayed photon analysis for a luminosity of 2 fb^{-1} and 10 fb^{-1} respectively taken from Ref. [19].

A Appendix-I: PRL Figures

Here we show the figures that are expected to go in the PRL. Note that they are the same content as Figures 12-(b), 16-(c), 17, and 18, but with PRL formatting.

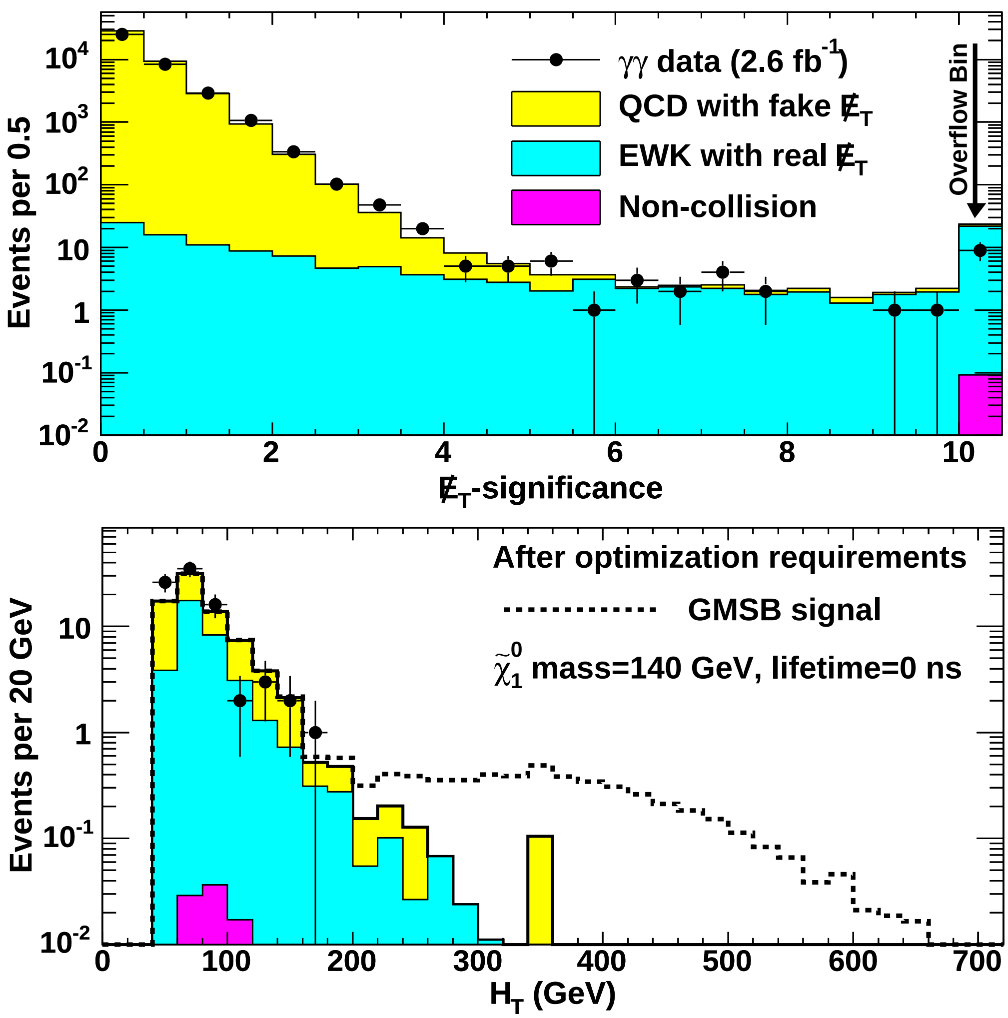

Figure 20: The top plot shows the $\not\!\!E_T$-Significance prediction for the $\gamma\gamma$ candidate sample after the preselection requirements along with the data, including predictions for all the backgrounds. The bottom plot shows the N-1 predicted H_T distribution after optimization, where the H_T is plotted through the whole region. There is no evidence for new physics and the data is well modeled by backgrounds alone.

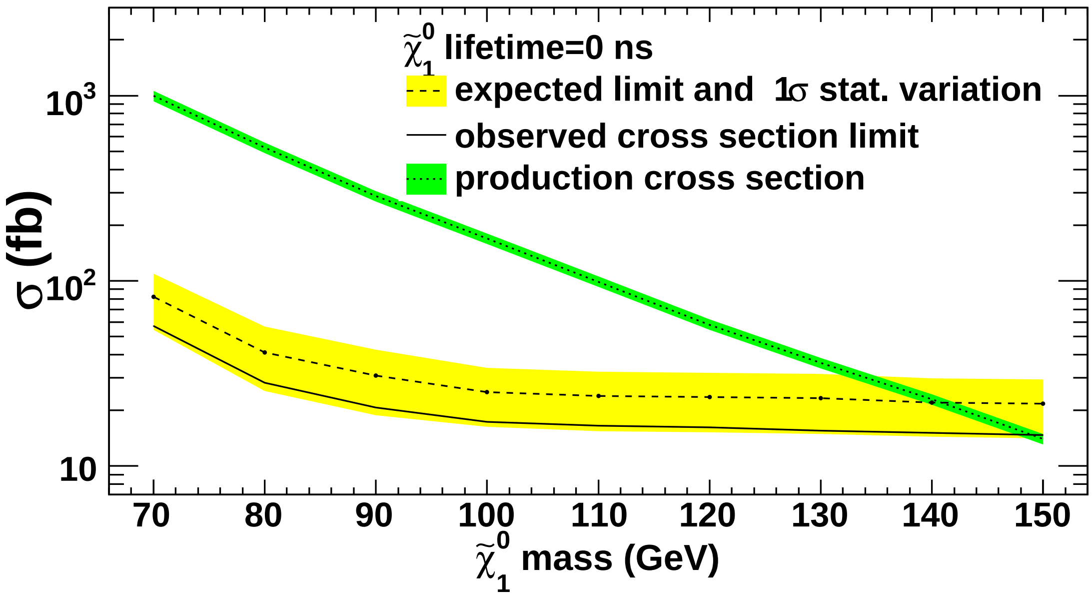

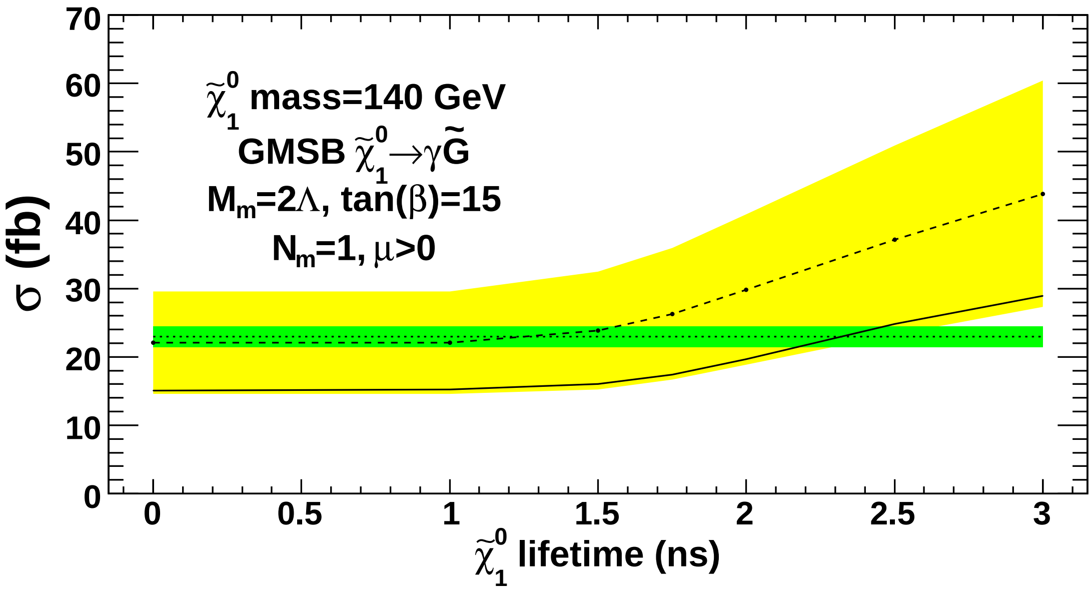

Figure 21: The predicted and observed cross section limits as a function of the $\tilde{\chi}_1^0$ mass at a lifetime of 0 ns (top) and as a function of the $\tilde{\chi}_1^0$ lifetime at a mass of 140 GeV/c^2 (bottom). Indicated in green is the 8.0% uncertainty-band for the production cross section, in yellow the RMS variation in the expected on the cross section limit.

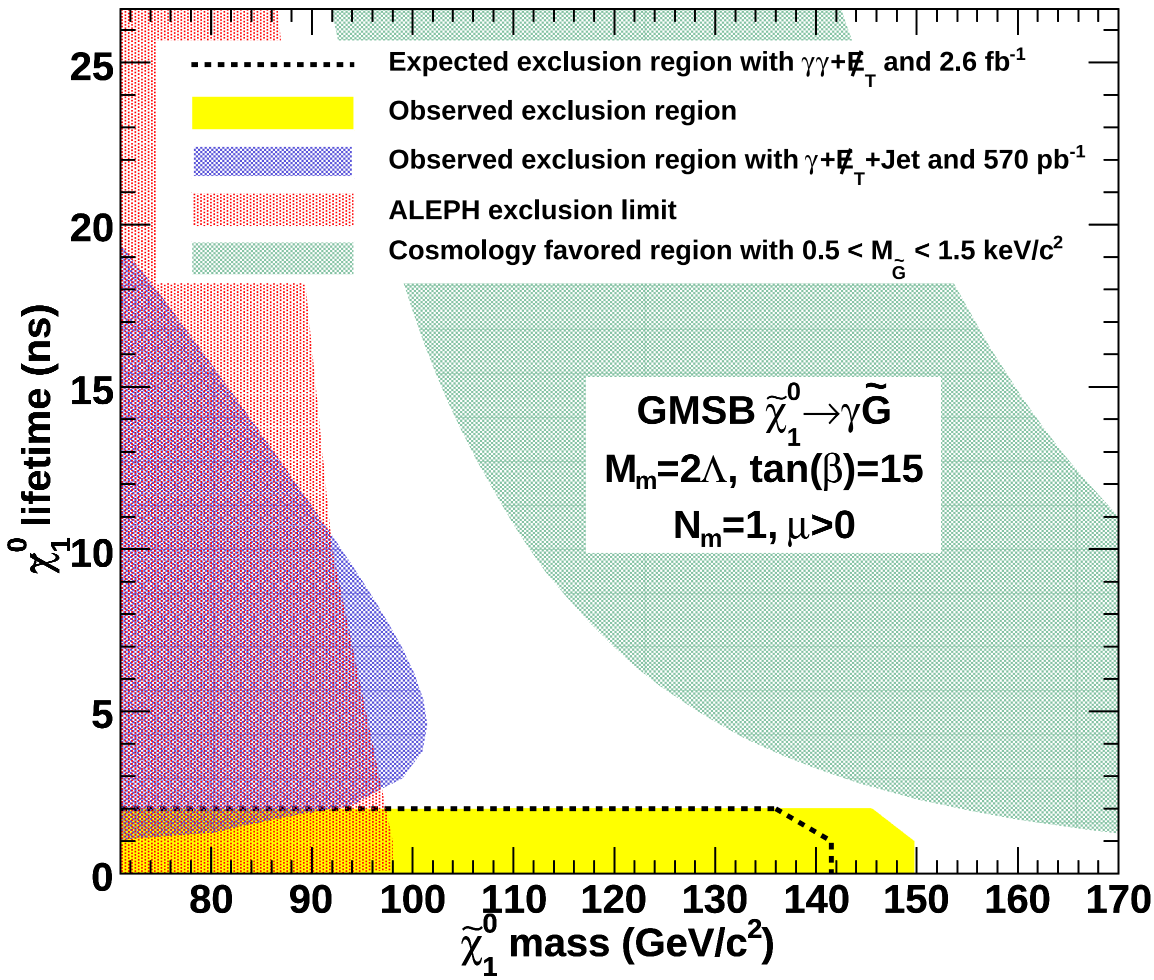

Figure 22: The predicted and observed exclusion region along with the limit from ALEPH/LEP [16] and the CDF $\gamma + \not\!\!E_T + jet$ delayed photon analysis [19]. We have a mass reach of 141 GeV/c^2 (predicted) and 149 GeV/c^2 (observed) at the lifetime up to 1 ns. The green shaded band shows the parameter space where $0.5 < m_{\tilde{G}} < 1.5$ keV/c^2, favored in cosmologically consistent models [4].

B Appendix-II: Changes Since the 2 fb^{-1} Analysis

The results of the search for GMSB models in the $\gamma\gamma + \not\!\!E_T$ final state with 2 fb^{-1} of data were blessed on November 6, 2008 as described in version 2.0 of this note. In this section, we present a brief summary of changes and improvements compared to the previous measurement.

- Added p12 - p17 data (1.0 fb^{-1}), which has high instantaneous luminosity, and dropped p0 data (0.4 fb^{-1}), which has low instantaneous luminosity and no EMTiming information. This change has the following consequences:
  - Now all data has the EMTiming information. This allows for a single set of simple and efficient ways to remove cosmic rays and beam halo events. We dropped the old inefficient, cosmic cuts.
  - Higher instantaneous luminosity increases the number of vertices per event, which results in larger contributions due to QCD wrong vertex. This, after re-optimization, is still small.
  - Higher instantaneous luminosity can potentially affect the acceptance. However, this has been checked and confirmed not to occur. See Appendix C.
- We added the PHO_50 and PHO_70 triggers to recover loss in efficiency for χ^2_{CES} at high photon E_T. With these additions we take the trigger efficiency to be 100%. For more detail see Appendix C. This leads to minimally larger trigger efficiencies and backgrounds, in particular, larger electroweak backgrounds. However, these changes are negligible after optimization.
- We realized we were not simulating the GMSB signal with Min-Bias. We now simulate the GMSB MC signal sample using PYTHIA with Tune-A and Min-Bias. These effects reduced the acceptance and thus the sensitivity from what was reported previously by a few percent.
- We reinstated the vertex swap procedure to remove wrong vertex events and added the $\not\!\!E_T$ cleanup cut to get rid of tri-photon events with a lost photon. We note this was inadvertently done for the background estimations in the previous analysis, but not for signal. Thus, our acceptance had been slightly overestimated relative to the backgrounds. Since the cuts are now part of the analysis they are correctly reported. We also confirmed that the vertex swap procedure and $\not\!\!E_T$ cleanup cut help the sensitivity.
- We added $Z \rightarrow \nu\nu$ to electroweak backgrounds. This adds about 20% more backgrounds after optimization. (N.B. This is done differently from version 3.0 of this note and what was blessed on 04/30/09)
- We combined the wrong vertex and triphoton QCD backgrounds into a single more inclusive pathology measurement.

- We finished our systematic studies. In the previous anaysis we used 18%, taken from 202 pb^{-1} analysis, [17] to be conservative. Now it is reduced to 10.6% since the uncertainty on photon ID and isolation efficiencies is smaller due to improved understanding of the detector [40, 41].

- We re-optimized after these changes and found that only the $\Delta\phi(\gamma_1, \gamma_2)$ cut needed to change from π-0.15 (2.99) to π-0.35 (2.79).

- We found that the formulae used to produce the cosmology favored region band in Figures 18 and 19 is incorrect. We now use Eq. (1) to correctly produce the band.

C Appendix-III: Trigger Efficiency and Luminosity Effects on the Acceptance

Figure 23 shows the E_T distributions of both photons in GMSB MC signal after the final kinematic cuts. With our combination of four triggers and over 99% of the events with $E_T^{\gamma 2} > 13$ GeV we take a trigger efficiency of 100% with negligible error [28].

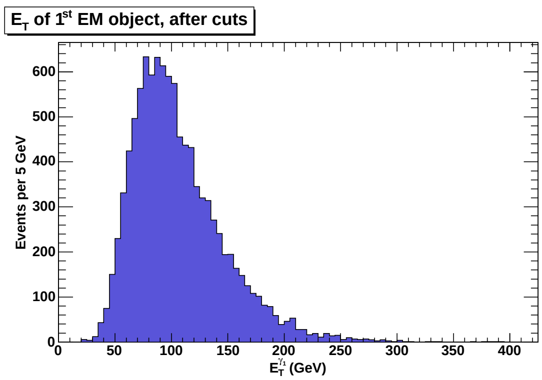

(a)

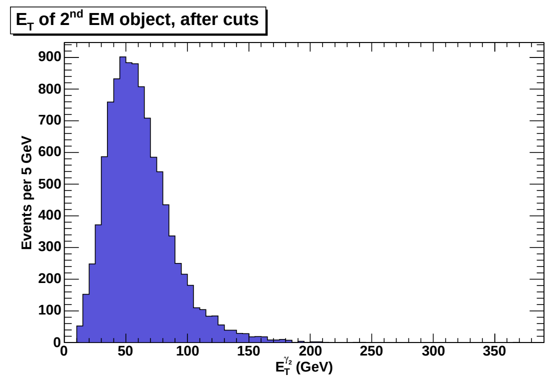

(b)

Figure 23: The photon E_T distributions for GMSB signal with $m_{\tilde{\chi}_1^0} = 140$ GeV and $\tau_{\tilde{\chi}_1^0} = 0$ ns after the final kinematic cuts. Well above 99% of our diphoton candidates are well above our $E_T > 13$ GeV threshold.

We simulate the GMSB signal using the detector calibrations of p1 to p13 for the PYTHIA MC sample with Tune-A and Min-Bias. We observe no acceptance dependence on the luminosty, thus we ignore additional systematics due to not including through p17. Figure 24 shows the efficiency curve. While the fit finds a small slope it is consistent with zero within errors. Note that most points are above the line, but the preponderance of the luminosity is in the later run periods.

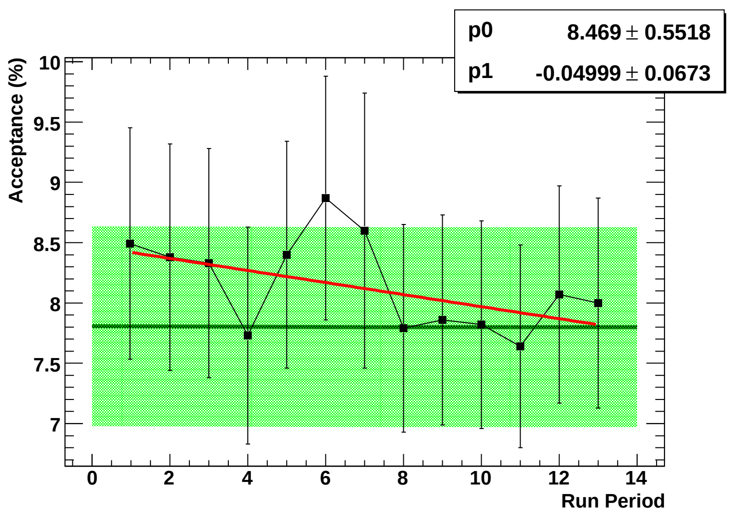

Figure 24: The signal acceptance as a function of luminosty. The slope (red solid line) from a linear fit has a small slope which is consistent with zero within uncertianty. The green solid line, with band, indicates the total signal acceptance.

References

[1] See for example, F. Halzen and A. D. Martin, "Quarks and Leptons," John Wiley & Sons, 1984; C. Quigg, "Gauge Theories of the Strong, Weak, and Electromagnetic Interactions," Addison-Wesley, 1983; and I. S. Hughes, "Elementary particles," Cambridge University Press, 1990.

[2] See for example S. Ambrosanio, G. L. Kane, G. D. Kribs, S. P. Martin and S. Mrenna, Phys. Rev. D **54**, 5395 (1996) or C. H. Chen and J. F. Gunion, Phys. Rev. D **58**, 075005 (1998).

[3] H. Baer *et al.*, FERMILAB-Pub-00/251-T, S. Dimopoulos *at al.*, SLAC-PUB-7236 (1996).

[4] J. L. Feng and T. Moroi, Phys. Rev. D **70**, 075019 (2004).

[5] P. Bode, J. Ostriker and N. Turok, Astrophys. J. **556**, 93 (2001).

[6] CDF Collaboration, F. Abe *et al.*, Phys. Rev. Lett. **81**, 1791 (1998); Phys. Rev. D **59**, 092002 (1999).

[7] P. Wagner and D. Toback, Phys. Rev. D **70**, 114032 (2004).

[8] M. Goncharov, V. Krutelyov, E. Lee, D. Toback, and P. Wagner, "Search for Heavy, Neutral, Long-Lived Particles that Decay to Photons", CDF Note 8016.

[9] In progress.

[10] B. C. Allanach *et. al.*, Eur. Phys. J. C**25**, 113 (2002).

[11] PYTHIA: T. Sjöstrand, L. Lönnblad and S. Mrenna, arXiv:hep-ph/0108264 (2001); *cdfsoft* 6.1.4 has PYTHIA version 6.216. *cdfSim*: G.S. Sganos, Tutorial on cdfSim. We modified it for the simulation of the EMTiming system [36]. It further includes a bug-fix of the tracking code to simulate the CES response to photons from displaced vertices correctly and a patch by A. Scott to include decay products of displaced $\tilde{\chi}_1^0$ in the detector simulation [37].

[12] W. Beenakker, *et al.*, Phys. Rev. Lett. **83**, 3780 (1999).

[13] P. Simeon and D. Toback, "An Advantage of Setting Cross Section Limits on the Total Production Mechanism When Multiple Processes Produce the Same Final State," CDF Note 7084 (2006).

[14] The remaining processes produce slepton pairs that also decay to pairs of $\tilde{\chi}_1^0$: τ_1 ($\sim 9\%$), e_R ($\sim 7\%$), μ_R ($\sim 7\%$).

[15] DØ Collaboration, B. Abbott *et. al.*, Phys. Rev. Lett. **80**, 442 (1998).

[16] ALEPH Collaboration, A. Heister *et. al.*, Eur. Phys. J. C **25**, 339 (2002); A. Garcia-Bellido, Ph.D. thesis, Royal Holloway University of London (2002) (unpublished), arXiv:hep-ex/0212024.

[17] CDF Collaboration, D. Acosta *et. al.*, Phys. Rev. D **71**, 031104 (2005).

[18] DØ Collaboration, V.M. Abazov *et. al.*, Phys. Lett. B **659**, 856 (2008).

[19] CDF Collaboration, A. Abdulencia *et. al.*, Phys. Rev. Lett **99**, 121801 (2007); CDF Collaboration, T.Aaltonen *et. al.*, Phys. Rev. D **78**, 032015 (2008).

[20] M. Goncharov *et. al.*, "The Timing System for the CDF Electromagnetic Calorimeters," CDF Note 7918 (2005), NIM A**565**, 543 (2006).

[21] R. Culbertson, M. Goncharov, and A. Pronko, "Search for Anomalous Production of $\gamma\gamma + \not\!\!E_T$ Events in 2 fb^{-1} of Data", CDF Note 9184.

[22] S. Jindariani *et al.,* "Luminosity Uncertainty for Run 2 up until August 2004", CDF Note 7446.

[23] http://www-cdf.fnal.gov/internal/physics/photon/goodrun.html, file goodrun_v17_pho_02.txt.

[24] http://www-cdf.fnal.gov/internal/dqm/goodrun/good.html, the script SAMLumi.ksh to compute luminosities for a given goorun list and dataset.

[25] Ray Culbertson *et al.,* "Search for Anomalous $\gamma\gamma + \not\!\!E_T$ Production and Limits on GMSB Models", CDF Note 6389.

[26] S-M Wynne, T. Berry, and R. Culbertson, "ID Efficiencies for Very High-Pt Photons", CDF Note 8302. For MC simulation the efficiency of the $\chi^2_{\rm CES}$ starts falling off at 100 GeV and starts dipping pretty seriously. However, the MC simulation is not accurate so it is more true that we just do not know what the efficiency is above the E_T scale of the Z events, where we can check it in data.

[27] http://www-cdf.fnal.gov/tiki/tiki-index.php?page_ref_id=57, Stntuple dev_243 build instructions.

[28] M. Dorigo and Shin-Shan Eiko Yu, "Diphoton Trigger Efficiency Study in 3 fb^{-1} of CDF II data", CDF Note 9533.

[29] CDF Collaboration, F. Abe *et al.*, Phys. Rev. Lett. **52**, 4784 (1995).

[30] R. Culbertson, A. Pronko, and Shin-Shan Eiko Yu, "The Probability of an Electron Faking an Isolated Prompt Photon in CEM", CDF Note 8220.

[31] M. Goncharov *et al.,* "Methods for Determining the Photon Event Rates and Timing Distributions for Searches with Final State Photons", CDF Note 7960.

[32] M. Goncharov *et al.,* "Discrimination of Beam Halo and Cosmic Rays as a Source of Photon Candidates", CDF Note 8409.

[33] CDF Collaboration, F. Abe *et al.*, Phys. Rev. Lett. **81**, 1791 (1998).

[34] http://www-cdf.fnal.gov/internal/physics/top/jets/systematics.html

[35] http://www-cdf.fnal.gov/physics/ewk/mc_samples.html

[36] M. Goncharov, V. Krutelyov, D. Toback and P. Wagner, "Resolution and Simulation of the EMTiming System", CDF Note 7928 (2006).

[37] M. Goncharov, D. Toback and P. Wagner, "Identification Efficiencies for Photons from Heavy, Long-Lived, Neutral Particles", CDF Note 7929 (2006).

[38] The ISASUGRA output is converted to PYTHIA using a script by A. Scott.

[39] R. Rossin, CDF Detector Lectures: "Systematics on the Luminosity Measurement", http://fcdfwww.fnal.gov/internal/WebTalks/Archive/0410/041007_clclum_detector_lecture/04_041007_clclum_detector_lecture_Roberto_Rossin_1_RobertoCLC_detector-04-10-07.pdf; S. Klimenko, J. Konigsberg and T. M. Liss, FERMILAB-FN-0741 (2003).

[40] C. Group, R. Culbertson, and J. Ray, "Photon Efficiency Scale Factor", CDF Note 9429 (2008).

[41] M. McFarlane, H. Bachacou, J. Nielsen, and W. Yao, "Study of High p_T Lepton Identification Efficiency Scale Factor and Related Cuts and Parameters in 5.3.3", CDF Note 7682 (2005).

[42] http://www-cdf.fnal.gov/internal/physics/joint_physics/agenda/20050527-minutes.html

[43] O. Gonzalez and C. Rott, "Uncertainties due to the PDFs for the gluino-sbottom search", CDF Note 7051 (2005).

[44] M. Griffiths *et. al.*, "Searches for Chargino and Neutralino in the e+e/mu+e/mu with 1 fb-1 of data", CDF Note 8389 (2006).

[45] see e.g. W. Beenakker, *et al.*, Nucl. phys. B **492**, 51 (1997); Prospino 2.0: http://www.ph.ed.ac.uk/∼tplehn/ prospino/prospino.html

[46] E. Boos, A. Vologdin, D. Toback and J. Gaspard, Phys. Rev. D **66**, 013011 (2002). J. Conway, CERN Yellow Book Report No. CERN 2000-005 (2000), p. 247.